Zeta-Payne: A Fully Automated Spectrum Analysis Algorithm for the Milky Way Mapper Program of the SDSS-V Survey

Ilya Straumit[1,2] ⓘ, Andrew Tkachenko[2], Sarah Gebruers[2,3], Jeroen Audenaert[2] ⓘ, Maosheng Xiang[3] ⓘ, Eleonora Zari[3],
Conny Aerts[2,3,4] ⓘ, Jennifer A. Johnson[1] ⓘ, Juna A. Kollmeier[5] ⓘ, Hans-Walter Rix[3] ⓘ, Rachael L. Beaton[5,6] ⓘ,
Jennifer L. Van Saders[7] ⓘ, Johanna Teske[8], Alexandre Roman-Lopes[9] ⓘ, Yuan-Sen Ting[10,11] ⓘ, and Carlos G. Román-Zúñiga[12] ⓘ

[1] The Department of Astronomy and Center of Cosmology and Astro Particle Physics, The Ohio State University, Columbus, OH 43210, USA;
ilya.straumit@kuleuven.be
[2] Institute of Astronomy, KU Leuven, Celestijnenlaan 200D, B-3001 Leuven, Belgium
[3] Max Planck Institute for Astronomy, Königstuhl 17, D-69117 Heidelberg, Germany
[4] Department of Astrophysics, IMAPP, Radboud University Nijmegen, PO Box 9010, 6500 GL Nijmegen, The Netherlands
[5] The Observatories of the Carnegie Institution for Science, 813 Santa Barbara Street, Pasadena, CA 91101, USA
[6] Department of Astrophysical Sciences, Princeton University, 4 Ivy Lane, Princeton, NJ 08544, USA
[7] Institute for Astronomy, University of Hawai'i, 2680 Woodlawn Drive, Honolulu, HI 96822, USA
[8] Earth and Planets Laboratory, Carnegie Institution for Science, 5241 Broad Branch Road, NW, Washington, DC 20015, USA
[9] Departamento de Astronomía, Facultad de Ciencias, Universidad de La Serena. Av. Juan Cisternas 1200, La Serena, Chile
[10] Research School of Astronomy & Astrophysics, Australian National University, Cotter Road, Weston, ACT 2611, Australia
[11] School of Computing, Australian National University, Acton ACT 2601, Australia
[12] Universidad Nacional Autónoma de México, Instituto de Astronomía, AP 106, Ensenada 22800, BC, México

Abstract

The Sloan Digital Sky Survey (SDSS) has recently initiated its fifth survey generation (SDSS-V), with a central focus on stellar spectroscopy. In particular, SDSS-V's Milky Way Mapper program will deliver multiepoch optical and near-infrared spectra for more than 5×10^6 stars across the entire sky, covering a large range in stellar mass, surface temperature, evolutionary stage, and age. About 10% of those spectra will be of hot stars of OBAF spectral types, for whose analysis no established survey pipelines exist. Here we present the spectral analysis algorithm, ZETA-PAYNE, developed specifically to obtain stellar labels from SDSS-V spectra of stars with these spectral types and drawing on machine-learning tools. We provide details of the algorithm training, its test on artificial spectra, and its validation on two control samples of real stars. Analysis with ZETA-PAYNE leads to only modest internal uncertainties in the near-IR with APOGEE (optical with BOSS): 3%–10% (1%–2%) for $T_{\rm eff}$, 5%–30% (5%–25%) for $v \sin i$, 1.7–6.3 km s^{-1} (0.7–2.2 km s^{-1}) for radial velocity, <0.1 dex (<0.05 dex) for $\log g$, and 0.4–0.5 dex (0.1 dex) for [M/H] of the star, respectively. We find a good agreement between atmospheric parameters of OBAF-type stars when inferred from their high- and low-resolution optical spectra. For most stellar labels, the APOGEE spectra are (far) less informative than the BOSS spectra of these stars, while $\log g$, $v \sin i$, and [M/H] are in most cases too uncertain for meaningful astrophysical interpretation. This makes BOSS low-resolution optical spectra better for stellar labels of OBAF-type stars, unless the latter are subject to high levels of extinction.

1. Introduction

Recent successes of space-based astrometric (e.g., Gaia, Gaia Collaboration et al. 2016) and photometric (CoRoT, Kepler, K2, and TESS; Auvergne et al. 2009; Borucki et al. 2010; Howell et al. 2014; Vanderspek 2019, respectively) missions implied a boost for stellar astrophysics. Nevertheless, (ground-based) stellar spectroscopy still occupies an important niche, thanks to the complementary nature of information it adds to the photometric and astrometric measurements. Indeed, even low-resolution ($R \sim 2000$–5000) spectroscopy offers an unprecedented level of detail in the analysis of stellar atmospheres as compared to (broadband) space-based photometric measurements, allowing us to resolve important diagnostic spectral lines and their blends.

Though space-based (photometric) missions deliver high-quality, high-duty cycle, and nearly uninterrupted time-series of data full of information, a considerable amount of stellar astrophysics applications, both at the level of individual objects and their ensembles, require precise atmospheric parameters and chemical compositions of stars, as well as estimates of their surface rotation and radial velocities. For example, (transiting) exoplanet studies often rely on ground-based spectroscopic measurements for the inference of planetary masses and properties of their host stars (e.g., Danielski et al. 2021). The study of planetary atmospheres through the method of transmission spectroscopy is another application (e.g., Kreidberg 2017; Limbach et al. 2020). Eclipsing binary studies also require spectroscopic observations to deduce masses and radii of both components with precision and accuracy better than the 3% level (e.g., Torres et al. 2010; Thomas et al. 2021; Serenelli et al. 2021), enabling stringent tests of stellar structure and evolution theory (e.g., Claret & Torres 2019; Tkachenko et al. 2020, and references therein). Furthermore, detailed astero-seismic studies of pulsating stars require knowledge of their

atmospheric chemical compositions and precise locations in the ($T_{\rm eff}$–log g) Kiel or ($T_{\rm eff}$–log L) Hertzsprung–Russell diagram, to enable observational probing of the physical conditions in the deep interiors of stars (e.g., Aerts et al. 2010; Aerts 2021).

Although detailed studies of individual objects are extremely important to assess the precision and accuracy of numerous theories and to provide recipes for their improvement, large-scale studies of (single, binary, and high-order multiple system) stars and their ensembles (open and globular clusters, star-forming regions, Galactic bulge, etc.) are vital to understanding the structure, dynamics, and evolution of galaxies (e.g., Zari et al. 2021). To that end, large-scale, all-sky, multiepoch ground-based spectroscopic surveys are irreplaceable both as a stand-alone mechanism for astrophysical studies as well as a complement to all-sky astrometric and photometric space missions like Gaia and TESS, respectively. To mention a few, the Sloan Digital Sky Survey (SDSS) has a two-decades long tradition in large-scale ground-based observations, starting with the SDSS-I survey devoted to imaging and spectroscopy of galaxies and quasars (Richards et al. 2002; Strauss et al. 2002), and now proceeding into its fifth phase/generation (SDSS-V, see Section 2) that will survey over five million stars in the Milky Way, study interstellar gas in the Galaxy and Local Group, and will track evolution of massive black holes growing at the centers of galaxies (Kollmeier et al. 2017). The Large Sky Area Multi-Object Fiber Spectroscopic Telescope (LAMOST) provides a large collection of low-resolution ($R \sim 1800$) spectra of stars of all spectral types through its Experiment for Galactic Understanding and Exploration survey of the Milky Way structure (e.g., Deng et al. 2012). Furthermore, the Gaia-ESO spectroscopic survey (Gilmore et al. 2012) targets over 10^5 stars in the Milky Way, complementing Gaia astrometric observations and providing the first homogeneous overview of the distributions of kinematics and elemental abundances in the galaxy. The GALactic Archaeology with HERMES (De Silva et al. 2015) survey aims to survey over a million stars of different ages and at different locations in the Milky Way to uncover its formation and evolution history. Last but not least, the WHT Enhanced Area Velocity Explorer (Bonifacio et al. 2016) and the 4 m Multi-Object Spectroscopic Telescope (de Jong et al. 2019) surveys allow for multiobject low- to medium-resolution spectroscopic observations, enabling chemical and kinematic studies of all components of the Milky Way, extragalactic science through observations of quasars, etc.

Analysis of this large volume of data is hardly a manageable task when relying on human power only. However, analysis by various machine-learning (ML)-based applications has proven to be rather easily accomplished by computers, provided the respective algorithms can be properly trained. For example, the Cannon APOGEE spectrum analysis pipeline (Ness et al. 2015; Casey et al. 2016) creates, from the spectra of reference stars with known stellar labels (e.g., $T_{\rm eff}$, log g, and [M/H]), a flexible generative model that describes a probability density function for continuum-normalized stellar flux as a function of the above-mentioned labels. The algorithm assumes that the continuum-normalized flux varies smoothly with the stellar labels, enabling fast and precise determination of stellar parameters from the previously unseen normalized spectra of the surveyed stars. The Cannon algorithm is often referred to as a "data-driven approach" owing to the limited model dependency that occurs only at the stage of the algorithm

training. Another example of, this time, a fully model-dependent ML-based approach is the (HOT)PAYNE (Ting et al. 2019; Xiang et al. 2021) algorithm that employs a neural network as an efficient predictor of (continuum-normalized) synthetic spectra. When teamed up with an optimization algorithm, the approach offers a fast way to analyze large volumes of spectroscopic data in the parameter space the neural network has been trained in. Even a higher level of data analysis is achieved with ML-based algorithms that employ the method of domain adaptation and offer a unique opportunity to improve theoretical models by learning from actual observations, as for example realized in the CYCLE-STARNET algorithm (O'Briain et al. 2021).

Any spectrum analysis starts with the most suitable processing of raw stellar spectra that includes optimal extraction (bias subtraction, flat-fielding, wavelength calibration, order merging in case of echelle spectra, etc.) and (optionally) normalization to the local continuum of the star. In medium- to large-scale surveys, where thousands to millions of stellar spectra have to be processed, optimal data processing requires dedicated data reduction pipelines, and the SDSS-V Milky Way Mapper (MWM) survey is no exception. As discussed in Kollmeier et al. (2017) and Section 2, MWM relies on the optical BOSS (Smee et al. 2013) and near-infrared APOGEE (Wilson et al. 2019) spectrographs to execute its science. Each of those instruments has a dedicated data reduction pipeline that delivers 1D, merged, wavelength, and flux-calibrated stellar spectra ready for a subsequent detailed astrophysical analysis and interpretation (Stoughton et al. 2002; Nidever et al. 2015).

Compared to most previous stellar spectroscopic surveys, MWM will take spectra of many different stars, from red giants to OBA-type stars, to cool YSOs and X-ray binaries. These cannot be modeled astrophysically with a single pipeline. Therefore, the MWM Survey employs an overarching software framework called ASTRA.[13] In a nutshell, ASTRA takes the 1D optimally reduced spectra as input, passes those through fully automated classifiers, makes an ML-based probabilistic decision on which data analysis pipeline(s) to call for that particular input spectrum, and collects and formats the pipeline's output, i.e., the stellar "labels" (e.g., $T_{\rm eff}$, log g, abundances, and multiplicity). To minimize the impact of possibly imprecise and/or erroneous classification, the three highest-probability classes are considered for each stellar spectrum that passes through the classification module of ASTRA.

In this paper, we build upon the legacy of the (HOT)PAYNE algorithm (Ting et al. 2019; Xiang et al. 2021) to develop an ML-based spectrum analysis method for the MWM program of the SDSS-V survey, with a particular focus on intermediate- and high-mass stars of spectral types O, B, A, and F, irrespective of whether those are observed with the BOSS low-resolution optical or the APOGEE medium-resolution near-IR instrument. Our algorithm is implemented in the ASTRA software framework and is employed for the analysis of spectra of OBAF-type stars targeted by MWM.

Section 2 provides a brief introduction to the SDSS-V survey and its MWM program, as well as a summary of the primary science questions that will be addressed with the sample of OBA(F)-type stars. Our spectrum analysis method is presented

---

[13] https://github.com/sdss/astra

in Section 3, where we describe and justify the changes made to the original (HOT)PAYNE algorithm, discuss the training process in detail, and introduce the optimization and statistical uncertainty determination framework. The algorithm is tested on simulated APOGEE and BOSS spectra in Section 4 and is further validated on low- to high-resolution spectra of real stars in Section 5. We conclude the paper with a discussion and future prospects presented in Section 6.

2. The SDSS-V and Milky Way Mapper Surveys

The SDSS-V survey has kicked off its observations in the fall of 2020 and will remain on sky for a total survey duration of up to 5 yr. SDSS-V is an all-sky, multiepoch survey whose spectroscopic observations will be acquired in the optical and near-IR wavelength domains with matched infrastructures in both hemispheres (Kollmeier et al. 2017). The survey serves as an umbrella for its three overarching scientific projects, called "Mappers": MWM, Local Volume Mapper (LVM), and black hole Mapper (BHM). In brief, the LVM survey[14] is an optical, integral-field spectroscopic survey that will target the mid plane of the Milky Way, Orion, and the Magellanic Clouds, using newly built telescopes operating at a resolving power of $R \sim 4000$. The ultimate goal of LVM is to address questions of star formation and physics of the interstellar medium through mapping the interstellar gas emission with unprecedented spatial resolution: subparsec in the galaxy, 10 parsec in the Magellanic Clouds, and <100 parsec out to distances of several megaparsecs. The BHM survey[15] will employ 2.5 m telescopes in both hemispheres, at Apache Point Observatory (Gunn et al. 2006) and at Las Campanas Observatory (Bowen & Vaughan 1973), to acquire multiepoch, optical low-resolution ($R \sim 2000$) BOSS spectroscopy of some 300,000 quasars. The ultimate goal of BHM is to understand the masses, accretion physics, and growth and evolution of supermassive black holes in the centers of galaxies.

The MWM survey[16] of SDSS-V will employ both the BOSS low-resolution ($R \sim 2000$) optical and the APOGEE medium-resolution ($R \sim 22,500$) near-IR spectroscopy. The survey will target over 4 million objects to provide a dense and contiguous stellar map across the sky but largely focused on low Galactic latitudes. High signal-to-noise ratio (S/N), medium-resolution near-IR spectra will be used to deduce stellar parameters and surface chemical composition of each star included in the program, providing the means to understand the dominant formation mechanisms of the Milky Way and its place in a cosmological context. The MWM survey will also make use of both optical and near-IR spectrographs to acquire multiepoch observations of tens of thousands multistar and planetary systems to understand formation, shaping, and evolution of (sub)stellar multicompanion systems. Last but not least, MWM will target stellar objects in a high-dimensional parameter space, including stellar mass, age, evolutionary status, chemical composition, rotation, and internal structure. Among the groups of stars that will be observed are young stellar objects, main-sequence stars, red giants, white dwarfs, low- ($M \lesssim 1.2\,M_\odot$), intermediate- ($1.2\,M_\odot \lesssim M \lesssim 8M_\odot$), and high-mass ($M \gtrsim 8\,M_\odot$) stars. The MWM survey will address a wide range of scientific questions, such as: true relationships between masses, radii, rotation, ages, and internal mixing of intermediate- to high-mass stars; precise age and chemical composition measurements of giant stars with asteroseismic detections; improved understanding of evolution of white dwarfs and their return to the interstellar matter; observations of deeply embedded stellar clusters and a volume-limited (within ~100 pc) census of stars in the solar neighborhood. We refer the reader to Kollmeier et al. (2017) for more information about the SDSS-V survey and its Mappers.

2.1. Intermediate- to High-mass OBA(F)-type Stars

The MWM survey of SDSS-V has a large science component devoted to intermediate- and high-mass stars of spectral types O, B, and A(F). Sample selection is done in the spirit of the SDSS-V requirement of a known and well-defined selection function, and is therefore based on Gaia EDR3 photometry and astrometry combined with the Two Micron All Sky Survey photometric information. First of all, the sample is restricted to sources with Gaia $G_{\rm mag} < 16$ due to the spectral-level requirement of the MWM survey that S/N of ~75 has to be reached with 15 minutes exposures with the BOSS instrument. Second, all objects whose absolute magnitude in the K photometric band is smaller than zero are selected, which roughly corresponds to a late B-type main-sequence star. Ultimately, several color cuts are applied to clean the sample from intrinsically bright red giant- and asymptotic giant-branch stars, as well as from objects with unnaturally blue colors. The final catalog comprises some $0.9M$ objects, where the fraction of O- and B-type stars is estimated to be close to 50%. The other half of the sample largely comprises A-type stars, though a small contamination from F-type stars cannot be excluded. More details about the target selection and estimation of the purity and completeness of the catalog are provided in Zari et al. (2021).

Following its science requirements, the MWM survey will deliver atmospheric properties of OBA(F)-type stars with precision better than 5%–10% for the effective temperature $T_{\rm eff}$, better than some 25%–30% for the projected rotational velocity $v \sin i$, ~0.1 dex for the surface gravity $\log g$, and ~0.15 dex for the bulk metallicity [M/H] and surface abundances of critical chemical elements such as He, C, N, O, Si, and Mg (perhaps more limited for the hottest O-type stars). With such a large sample of multiepoch spectra, we can probe:

1. The intrinsic variability (stellar pulsations, rotational modulation, quasiperiodic variability, etc.), internal properties (interior rotation and mixing, convective core masses, etc.), and ages of intermediate- to high-mass stars, thanks to synergy with the Kepler and TESS space-based photometric surveys. For example, we will be able to better assess fractions of Ae/Be stars and magnetic intermediate- to high-mass stars, where the latter can be unraveled by indirect means through photometric detections of rotational modulation and spectroscopic inferences of surface chemical abundance anomalies. Stellar pulsations will be used in combination with spectroscopically inferred atmospheric parameters to learn about internal physical properties of stars, using well-established asteroseismic methods (Aerts et al. 2018, 2019; Aerts 2021). In particular, it was recently demonstrated that internal rotation and mixing properties of B-type main-sequence stars can be readily inferred from a

combined asteroseismic and spectroscopic analysis (e.g., Pápics et al. 2017; Pedersen et al. 2018, 2021). Moreover, Bowman et al. (2019, 2020) demonstrated that high-mass O-type stars and evolved B-type supergiants also hold strong asteroseismic potential even at metallicities as low as that of the LMC, thanks to the observational detection of low-frequency stochastic variability such as the one caused by internal gravity waves excited at the interface of convective and radiative regions near the stellar core (Edelmann et al. 2019; Horst et al. 2020);

2. Binary and multiplicity fractions among intermediate- to high-mass stars across the sky and as a function of metallicity (galaxy versus Magellanic Clouds). Sana et al. (2012, 2013) found a large fraction of binaries among massive stars and hypothesized that almost all high-mass stars have gone through some sort of binary interactions in the course of their evolution. Notably, Almeida et al. (2017) reported some 60% observed binary fraction among O-type stars in the 30 Dor region of the LMC, while Bodensteiner et al. (2021) and Banyard et al. (2022) found similar binary fractions for B-type stars in the SMC and galaxy, respectively. Luo et al. (2021) reported a comparable binary fraction of ∼40% from their study of some 330 OB-type stars observed by LAMOST having at least three spectroscopic epochs. The MWM Survey of SDSS-V will deliver optical and near-IR measurements for a three-orders-of-magnitude-larger sample of OBA(F)-type stars, thus allowing for a homogeneous search for binary and higher-order multiple systems in the galaxy and Magellanic Clouds; and

3. The structure of the galaxy as revealed by its young stellar components, in particular the kinematics, dynamics, and nature of the Galactic spiral arms. Zari et al. (2021) demonstrated that the structure of the Milky Way as traced with young OB-type stars is not necessarily the same as deduced from observations of red giants, from analysis of the distribution of dust in the galaxy, or from the distributions of Cepheids and/or masers (see also Poggio et al. 2021). The authors found that the distribution of OBA-type stars in the plane is highly structured, with pronounced over- and under-densities, and conclude that young stars in the galaxy are not neatly organized into distinct spiral arms. In agreement with previous studies of OB-type stars in the literature, Zari et al.'s (2021) findings might point either to a more flocculent structure of the Milky Way at optical wavelengths or to the fact that star formation occurs in a clumpy and patchy fashion. The authors emphasize that better-quality Gaia DR3 data and spectroscopic information from the SDSS-V survey will allow them to assess different models of spiral arms and shed light on their nature.

3. Spectrum Analysis Algorithm

As was briefly mentioned in Section 1, we aim to develop an efficient spectrum analysis algorithm for the MWM survey of SDSS-V, with the primary focus on intermediate- to high-mass stars of spectral types O, B, A, and F. One of the main requirements at this stage is a wide applicability range of the algorithm in terms of the wavelength coverage and resolving power of the obtained spectra, and without the need for human intervention between data reduction pipelines and spectrum analysis itself. Here, we use the heritage of one of the publicly available ML-based methods, namely the (HOT)PAYNE algorithm (Ting et al. 2019; Xiang et al. 2021), to which we introduce a number of modifications to comply with the aforementioned primary requirement of MWM.
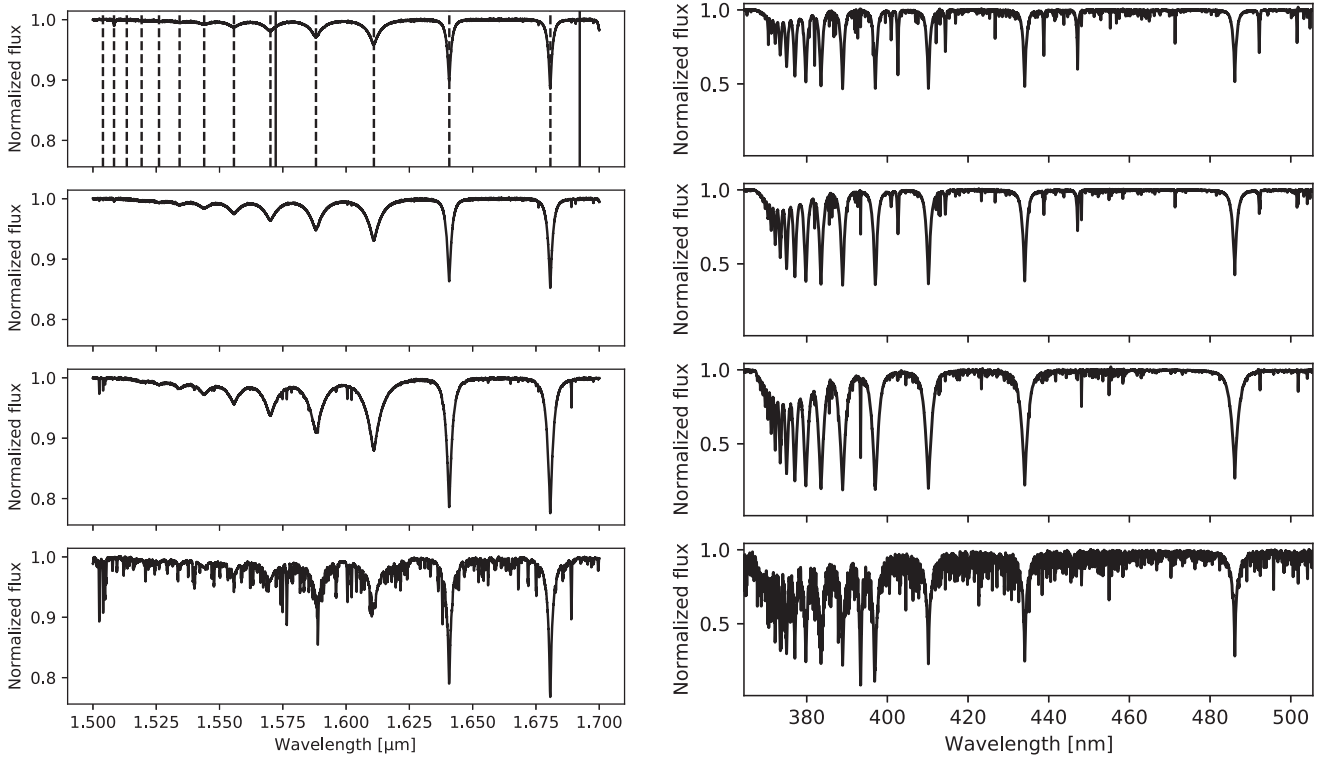
It is quite common to use optical low- to high-resolution spectra to deduce atmospheric parameters of intermediate- to high-mass OBAF-type stars, unless there is an interest in, e.g., specific UV lines to study winds of massive stars. On one hand, optical spectra of late-type stars will often contain important diagnostic lines of hydrogen (the Balmer series) and/or helium, a large number of metal lines (e.g., C, N, O, Mg, Si, and Al), and (in many cases) quite well-defined regions of pseudo-continuum, making it possible to achieve high-quality spectrum normalization. To give a few examples, methods such as Spectroscopy Made Easy[17] (Valenti & Piskunov 1996; Piskunov & Valenti 2017), Grid Search in Stellar Parameters[18] (GSSP; Tkachenko 2015), and the DETAIL (Giddings 1981) and SURFACE (Butler 1984) suite of codes, are all designed to work with continuum-normalized observed spectra and are most often applied in the optical wavelength range. On the other hand, use of near-IR spectra for the analysis of intermediate- to high-mass stars is rather scarce owing to few diagnostic (metal) lines occurring at those wavelengths and to problems associated with often uncertain normalization of spectra to the pseudo-continuum. Roman-Lopes et al. (2018) demonstrated that the APOGEE near-IR spectra (wavelength coverage from 1.5 to 1.7 μm) of OB-type stars are rather featureless and display exclusively hydrogen lines of the Brackett series and at most two He II lines at higher temperatures corresponding to O-type stars. The authors, alongside Ramírez-Preciado et al. (2020), developed a (semi) empirical spectral classification method for hot OB-type stars based on equivalent width measurements of key spectral lines in the APOGEE spectra, and making use of the San Pedro Martir observatory instrument medium-resolution and LAMOST survey low-resolution optical spectra, respectively, to benchmark their relations. Their method has recently been extended and applied to the APOGEE spectra of cooler A-type stars (Ramirez-Preciado et al., in revision).

Here, we aim to develop a spectrum analysis approach that can be applied to APOGEE spectra of OBAF-type stars (where a high density of hydrogen lines prevents precise normalization of spectra to the local continuum) and to BOSS optical spectra without the need for a substantial modification of the algorithm. That said, specifics of the APOGEE near-IR spectra of OBAF-type stars is what drives our definition of the model spectrum as described in Section 3.1. However, it does not mean that we value the medium-resolution near-IR spectra more than their low-resolution optical counterpart. On the contrary, as we demonstrate and conclude in Sections 5 and 6, respectively, low-resolution optical spectra of OBAF-type stars will often contain more information than medium-resolution near-IR spectra of these objects; hence, both types of data deserve our attention in equal proportions.

---

[17] https://www.stsci.edu/~valenti/sme.html
[18] https://fys.kuleuven.be/ster/meetings/binary-2015/gssp-software-package

Figure 1. Left: normalized synthetic spectra of (from top to bottom) OBAF-type stars computed with the GSSP software package in the APOGEE wavelength range. Vertical dashed lines in the top plot indicate positions of hydrogen lines of the Brackett series, while vertical solid lines mark positions of the He II lines at 1.5722 μm and 1.6923 μm, whose wavelengths are taken from Lenorzer et al. (2004). Right: normalized synthetic spectra for the same stellar parameters in the BOSS wavelength range (only part of the full range is shown for clarity).

3.1. Representation of a Model Spectrum

A fully automated analysis of the APOGEE near-IR and BOSS optical spectra of OBAF-type stars in the entire wavelength range requires a careful treatment of pseudo-continuum in the model. As demonstrated in Figure 1 (left panel), the high density of hydrogen lines in the near-IR part of the stellar spectrum, combined with the (typically) moderate- to high rotation of OBAF-type stars, makes determination and placement of the pseudo-continuum extremely difficult, and in the case of hotter OB-type stars, often impossible. The same is true for the BOSS optical spectra when the most blue and red parts of the spectrum are included in the analysis, where hydrogen lines of, respectively, the Balmer and Paschen series, start merging together. In addition, even when the above-mentioned wavelength intervals are omitted in the analysis, the remaining wavelength range of the BOSS instrument is sufficiently wide to observe significant variations that are instrumental in origin. Therefore, we incorporate a theoretical function into the model spectrum that aims to account for instrumental effects, possible interstellar reddening, and local stellar continuum, thus eliminating the need to process the input observed spectrum in a way beyond its optimal extraction. The instrumental effects that are taken into account in the model are: (i) the wavelength-dependent residual response function of the instrument that produces a large-scale distortion of the observed spectrum, and (ii) the line-spread function (LSF) that causes blurring of spectral lines in the observed spectrum. Observed spectra in the APOGEE entire wavelength range and the BOSS red part of the spectrum are rich in telluric contributions that are removed by the data

reduction pipeline using observations of telluric standard stars (typically, rapidly rotating stars of spectral types B and A; Nidever et al. 2015). Thus, a general model of a stellar spectrum, as it comes out of the SDSS data reduction pipeline(s), can be written down as follows:

$$\text{Flux} = \text{LSF} * [\prod_i \text{Line}_i(T_{\text{eff}}, \log(g),...)] \times \text{Response}(\lambda).$$

(1)

Here, LSF is the line-spread function, Line_i are the spectral lines formed in the stellar photosphere characterized by a set of parameters T_{eff}, $\log g$, $v \sin i$, [M/H], and v_{micro} (microturbulent velocity), and $\text{Response}(\lambda)$ is a wavelength-dependent theoretical function that accounts for instrumental effects, interstellar reddening, and local stellar continuum contributions. For simplicity and hereafter, we dub the $\text{Response}(\lambda)$ the "residual response function." We include two options to account for the LSF of the instrument, a simplified approach where the LSF is represented by a wavelength-independent Gaussian kernel with the FWHM corresponding to a given resolving power R of the instrument, and a detailed wavelength-dependent model of the LSF that will also be variable from fiber to fiber. The latter is usually estimated from a spectrum of the wavelength calibration unit and is available for both instruments (i.e., BOSS and APOGEE) of the MWM survey. The residual response function is modeled as a series of
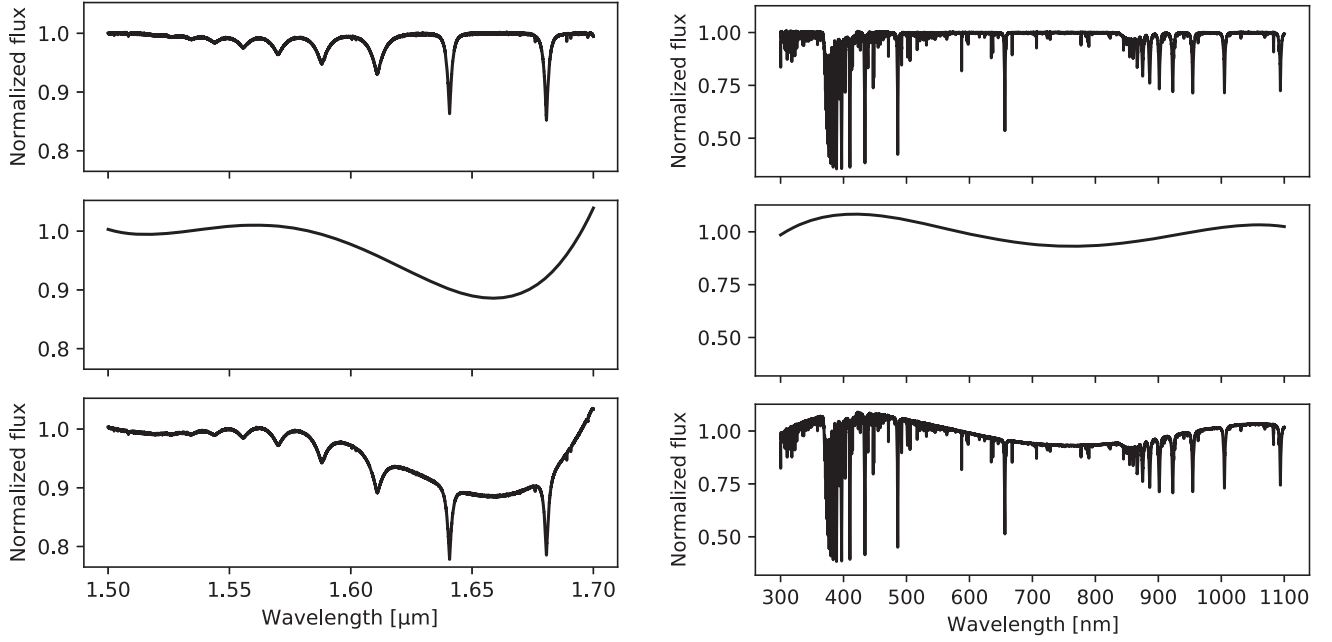
Figure 2. From top to bottom: synthetic APOGEE (left) or BOSS (right) spectrum of a B-type star, random fifth-order Chebyshev polynomial (model of the unknown response function), and a product of the synthetic spectrum with the model of the response function.

Chebyshev polynomials, i.e.,

$$\text{Response}(\lambda) = \sum_i c_i T_i(\lambda), \qquad (2)$$

where c_i are the coefficients of the series, T_i are the Chebyshev polynomials of the first kind, and λ is the wavelength. Figure 2 shows a representative example of the model spectrum of a B-type star in the APOGEE (left) and BOSS (right) wavelength ranges. The normalized synthetic spectrum, a model of the residual response function, and their product are shown in the top, middle, and bottom panels, respectively.

3.2. Neural Network Configuration, Training, and Validation

Following Ting et al. (2019), we use a neural network to approximate a grid of model spectra, where the neural network essentially acts as an efficient interpolator in the parameter space defined by the pre-computed grid of models. The main purpose of using a neural network is to make the model spectra differentiable by the stellar parameters, which allows us to perform optimization instead of a full grid search. Aside from that, the neural network is trained on a quasi-random grid as defined in Sobol (1967), which is more time efficient than computing a full grid of model spectra with the same parameter range. At present, we use the GSSP software package (Tkachenko 2015) to compute a grid of models required for the neural network training. GSSP employs a grid of plane-parallel atmospheric models pre-computed with the LLMODELS code (Shulyak et al. 2004) coupled to the SYNTHV (Tsymbal 1996) line formation code to calculate synthetic spectra in an arbitrary wavelength range. Both codes rely on the local thermodynamical equilibrium (LTE) approximation and include the option to compute the atmospheric structure and detailed line formation for a user-specified chemical composition pattern (including vertical stratification of elements in the stellar atmosphere, if necessary).

Table 1
Parameters of the Training Sets Used for Training Neural Networks in This Study

| Parameter | Near-IR | Optical | |
	APOGEE	BOSS	HERMES
Wavelength range, Å	15,000...17,000	3600...10,400	4200...5800
Wavelength step, Å	0.05	0.06	0.015
Number of models	5000 Sobol + 5000 Gaussian		
T_{eff}, K	Sobol(6000...25000) + Gaussian(6000, 3000)		
log g, dex	Sobol(3.0...5.0)		
$v \sin i$, km s^{-1}	Sobol(0...400) + Gaussian(0, 25)		
[M/H], dex	Sobol(−0.8...0.8)		

Note. See the text for details.

The neural network consists of two layers of neurons with "leaky ReLU" (leaky rectifier linear unit) activation function, which is defined as follows:

$$g(x) = \begin{cases} x & \text{if } x > 0, \\ 0.01x & \text{otherwise.} \end{cases} \qquad (3)$$

Once the neural network has been trained, it takes stellar parameters normalized to the range [−0.5, 0.5] as input and returns the corresponding synthetic spectrum as the output. This means that the number of the neural network outputs is equal to the number of spectral channels in the training set of synthetic spectra. Theoretical spectra for the training set are computed at infinite resolving power and cover wavelength ranges of the SDSS-V BOSS and APOGEE instruments, i.e., 3600–10400 Å and 1.5–1.7 μm, respectively. Table 1 provides a summary of the properties of the training set in terms of the total number of models used, wavelength range coverage, and definition of the parameter space. The network is implemented
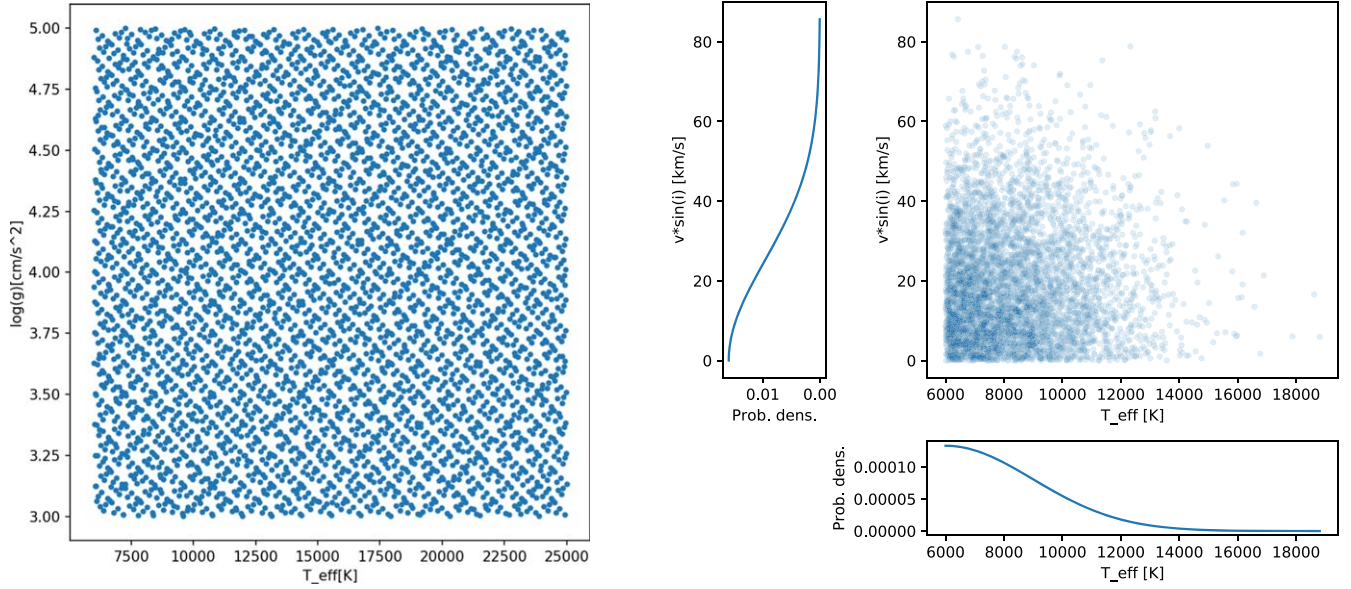
Figure 3. Left: a quasi-random grid of synthetic APOGEE spectra, projected onto the T_{eff}–$\log g$ plane. Right: an additional random sample of models to increase the density of the grid in the low T_{eff}–$v \sin i$ region. The probability density functions for T_{eff} and $v \sin i$ from which the points are sampled are shown in the left and bottom panels, respectively.

and trained with the TORCH framework using the RADAM optimization algorithm discussed in detail in Liu et al. (2019).

We note that the optical wavelength range specified for the HERMES instrument in Table 1 that we use for the algorithm validation in Section 5 is shorter than its full wavelength coverage from 3770–9000 Å. This is due to the memory limitation of the computing device currently used for the training, as the large number of models and the fine wavelength step of 0.015 Å dictated by the high-resolution of the HERMES instrument do not allow us to train a neural network for the full wavelength range. We choose to work with the wavelength interval from 4200–5800 Å for the following reasons: (1) it includes spectral lines of hydrogen from the Balmer series (H_γ, and H_β), and in case of hotter OB-type stars, several spectral lines of helium, which are usually employed as the main diagnostic lines for determination of the effective temperature and surface gravity of OBAF-type stars (Massey et al. 2009), (2) it also includes a plethora of metal lines that serve as the main diagnostic for the inference of the metallicity and projected rotational velocity (and extra line broadening parameters, if applicable) of the star, and (3) parts of the HERMES optical spectrum blue- and redward of the chosen wavelength interval suffer from high levels of noise and large contributions from telluric lines, respectively. Finally, because we (in particular) perform a comparative analysis between high- and low-resolution optical spectroscopy in this work (see Section 5 for details), the exact overlap between the two types of data in terms of the considered wavelength interval is much more critical than the exact length of the interval used, unless it is unrealistically short (which is not the case here).

For the training set, we ultimately use a hybrid grid that consists of a combination of a quasi-random Sobol grid that covers the entire parameter space of interest and an additional random grid sampled from a Gaussian distribution in a restricted region of the parameter space, as demonstrated in Figure 3. A quasi-random Sobol grid has the useful property that it covers the parameter space uniformly regardless of the number of points in the grid, unlike a true random uniform distribution, which may produce "clumps" of points and regions of the parameter space that are poorly sampled. The need for a hybrid grid arises from inferior performance of the neural network in the APOGEE wavelength range in the regime of slowly rotating late A- to F-type stars ($T_{eff} \lesssim 10,000$ K and $v \sin i \lesssim 30$ km s^{-1}) when it is trained on a quasi-random Sobol grid only. The low performance of the neural network in this regime is associated with a high (morphological) complexity of stellar spectra that are found to exhibit a large number of narrow spectral lines of metals as compared to spectra of hotter and more rapidly rotating stars (see, e.g., a comparison between APOGEE spectra of B- and F-type stars in Figure 1). When trained exclusively on a quasi-random Sobol grid (see left panel in Figure 3), the neural network does not have enough examples of highly complex spectra and experiences performance difficulties in the corresponding region of the parameter space. Adding a random sample of models from a Gaussian distribution $T_{eff} \sim N(6000, 3000)$, $v \sin i \sim N(0, 25)$ (see right panel in Figure 3) resolves the issue and equalizes the neural network performance across the entire parameter space. The grid used for training the neural network eventually consists of 10,000 models, equally split between the Sobol quasi-random and extra random grids.

Training of the neural network is performed in an iterative fashion. The combined grid of 10,000 models is split into training and validation sets, where the former comprises 90% of models, while the latter contains the remaining 10%. Note that the validation set is different from the test set, which is used to evaluate performance of the network after it is trained (Section 4); the test set is generated separately from the validation set. At every iteration, the neural network coefficients are optimized based on the training set using the RADAM optimization algorithm. The training is done in batches of 1000 models, selected randomly from the training set of models; the number of batches used at every iteration equals the total number of models in the training set divided by the batch size. Every 100th iteration, a score is calculated based on the validation set, and if the new score is better than any of the
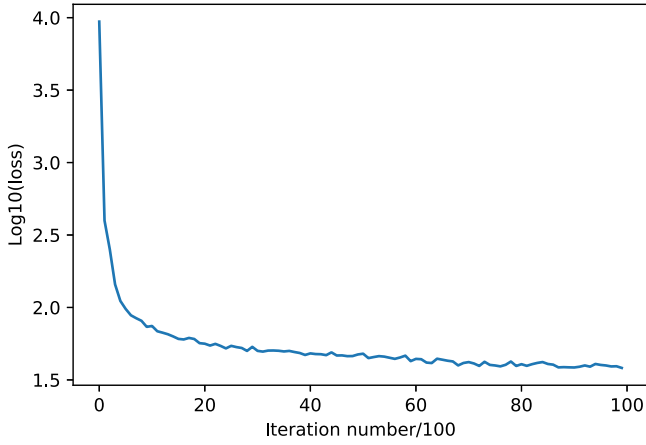
Figure 4. Score as a function of iteration number during the training of a neural network.

previous scores, the network weights are saved into a file. This process is run for a fixed number of 10^4 iterations that we found experimentally to be sufficient for the convergence. Figure 4 shows the evolution of the score during the neural network training process.

3.3. Model Fitting and Parameter Statistical Uncertainty

The best stellar parameters for an input observed spectrum are found by performing minimization of the χ^2 merit function defined as:

$$\chi^2 = \sum_i \left(\frac{f_i - F(\theta, \lambda_i)}{\sigma_i} \right)^2. \quad (4)$$

Here, f_i represents the observed fluxes with errors σ_i, θ is the stellar parameter vector, and λ_i is the wavelength grid. $F(\theta)$ is the model spectrum defined as:

$$F(\theta) = \{LSF * D[NN(\theta, \lambda_i), v_r]\} \times R(\lambda_i), \quad (5)$$

where $NN(\theta, \lambda_i)$ is the neural network output for stellar parameters θ, the operator $D[\cdot, v_r]$ performs a Doppler shift of the input observed spectrum according to the radial velocity v_r, and $R(\lambda_i) = \text{Response}(\lambda)$ represents the residual response function as defined in Equation (2).

Optimization of the objective function is done using the "Trust Region Reflective" method discussed in Branch et al. (1999). In the first instance, we use the central point of the parameter space of the neural network training set to initialize the optimization algorithm, and investigate the algorithm convergence properties based on artificial spectra of OBAF-stars. These tests reveal a nonnegligible number of cases where the optimization algorithm gets stuck in a local minimum located in an incorrect region of the parameter space. The most common failures of the optimization algorithm are associated with it getting stuck above or below T_{eff} of some 10,000 K, and this divergence of the algorithm is most pronounced for the APOGEE near-IR spectra. We solve the issue by providing the algorithm with a better (lower χ^2) initial guess for the (stellar) parameters vector instead of consistently using the central point of the neural network training grid. In order to find a better starting point for the optimization, we first perform a global (pre-)search by visiting a number of points in the stellar parameters space, passing the value of the parameters at a given point to the neural network and checking the value of χ^2 at

every point, with the aim of finding the point that achieves the lowest χ^2. In order to make the search scalable for different numbers of points (currently we set it to 4000), we use the Sobol algorithm to generate the set of points to visit, so that it covers the parameter space uniformly.

The preliminary search is performed in the space of stellar parameters and radial velocity. Because the main purpose of the pre-search step is to locate a sensible initial guess in the fastest possible way, we decouple modeling of the residual response function from the stellar parameter and radial velocity estimation at this stage. This way, we first perform a run of the optimization algorithm starting from a point in the center of the parameter space, which provides a first estimate for a vector of the Chebyshev coefficients that describe the residual response function. This set of coefficients is then used to perform a pre-search in the stellar parameter space (including radial velocity). After that, a point corresponding to the lowest χ^2 merit function is identified as the most suitable initial guess for the input (observed) spectrum. The identified initial guess is then applied in a final round of optimization in the combined space of stellar parameters and Chebyshev coefficients, to derive their optimal values and functional form for the observed spectrum in question.

The statistical uncertainty of the stellar parameters is calculated by fitting a second-degree polynomial to the χ^2 distribution for each of the parameters, which is equivalent to assuming a Gaussian form of the posterior probability distribution. Due to the finite resolving power of the instrument, the spectrum has fewer degrees of freedom than the number of spectral bins. To account for this, we calculate the effective number of degrees of freedom as follows:

$$N_{\text{deg}} = 4R \frac{\lambda_{\text{end}} - \lambda_{\text{start}}}{\lambda_{\text{start}} + \lambda_{\text{end}}}, \quad (6)$$

where R is the resolving power of the instrument, while λ_{start} and λ_{end} determine the wavelength range covered by the spectrum. The effective number of degrees of freedom N_{deg} is used to compute the 1σ statistical uncertainty level in terms of χ^2:

$$\chi^2_{1\sigma} = 1 + \sqrt{2/N_{\text{deg}}}. \quad (7)$$

Ultimately, the statistical uncertainty interval for the parameter in question is found from the intersection points of the second-order polynomial fitted to the χ^2 distribution with the horizontal line drawn at $\chi^2_{1\sigma} \cdot \chi^2_{\text{min}}$, where χ^2_{min} is the minimum value of the second-order polynomial.

4. Performance of the "ZETA-PAYNE" Algorithm on Simulated Data

In order to evaluate the internal uncertainty for stellar parameters intrinsic to the developed modeling framework in Section 3, we perform a simulation study where a 1000 artificial APOGEE and BOSS spectra are generated and subsequently processed as if they were observations of real stars. The simulated spectra are created on the actual APOGEE and BOSS wavelength grids, covering a wavelength range from 1.5–1.7 μm and from 3600–10400 Å, respectively. For APOGEE spectra, we also introduce two wavelength gaps between CCD sensors to resemble real observations as close as possible. The spectra for these simulated data sets are generated with the GSSP software package and for a random set of stellar

8
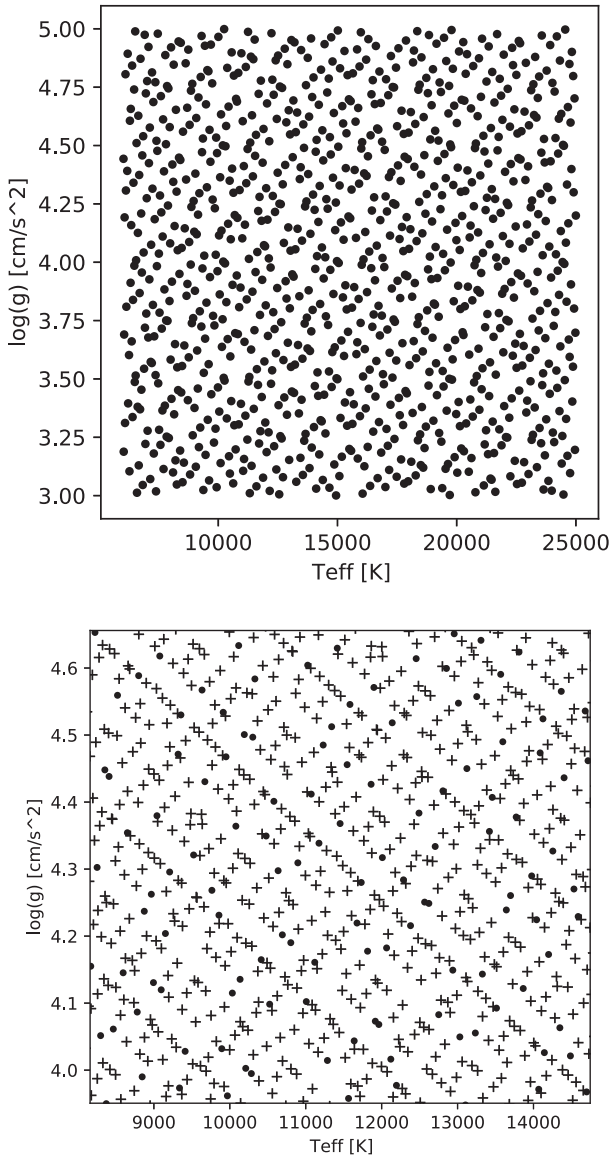
Figure 5. Top: the T_{eff}–$v \sin i$ distribution of the 1000 simulated spectra that are used to estimate the internal uncertainty. Bottom: comparison of the training (crosses) and test (dots) grids. See the text for details.

parameters. The spectra are shifted in wavelength according to a random radial velocity (uniformly distributed from -50 to 50 km^{-1}), convolved with a Gaussian function to simulate limited spectral resolution of the instrument ($R \approx 22{,}500$ and 2000 for APOGEE and BOSS, respectively), and multiplied by a random fifth-order Chebyshev series imitating the instrumental response function. Finally, Poisson noise is added to the spectrum to simulate varying quality levels of observations in terms of S/N, where we consider the cases of S/N $= \infty$ (noiseless artificial data), 100, and 50.

The sets of simulated APOGEE and BOSS spectra are generated to have a uniform density in the parameter space. The sampling is done using a quasi-random (Sobol) algorithm in the stellar parameter space and is assumed to be the same for both instruments (see top panel in Figure 5 for the projection of the data set on the T_{eff}–$v \sin i$ plane). This way, we are not only able to quantify the parameter internal uncertainties in both

wavelength ranges, but also to perform a cross-validation between the medium-resolution near-IR and low-resolution optical regimes. We also make sure that the test data set has zero overlap with the neural network training set (see bottom panel in Figure 5).

The mock spectra are analyzed with the ZETA-PAYNE algorithm, and the internal uncertainty is calculated as follows: (i) a difference in the true versus predicted parameter value $\Delta\theta$ is calculated, and the 16th, 50th, and 84th percentiles (further labeled as P_{16}, P_{50}, and P_{84}, respectively) of the obtained distributions are computed; (ii) models with the parameter value differences satisfying the criterion $4(P_{50} + P_{16}) < \Delta\theta < 4(P_{50} + P_{84})$ are selected as achieving a satisfactory fit of the model to the mock spectrum, while the rest are classified as failing to converge to the correct model. The internal uncertainty is then calculated based on the converged models. Thus the performance of the method is characterized by the internal uncertainty as well as by the reliability metric, i.e., the probability that the optimization algorithm converges to a correct value. The internal uncertainty reflects (i) how well the neural network is able to predict synthetic fluxes for a given set of stellar labels, and (ii) how good the performance of the chosen minimization algorithm is in finding and converging to the global minimum in the parameter space.

Results of the application of the ZETA-PAYNE algorithm to the set of 1000 artificial noiseless APOGEE spectra are summarized in Figure 6, where we compare the parameters inferred from the simulated data with their true values. The differences between the inferred and true parameter values are presented for (from top to bottom) T_{eff}, $\log g$, $v \sin i$, and [M/H], and as a function of true T_{eff} (left column) and $v \sin i$ (right column). In each panel in Figure 6, we divide the corresponding data set into 10 equal-width bins and compute the internal uncertainty in each of those bins as described above. The resulting internal uncertainties per parameter bin are shown as magenta full circles with error bars in Figure 6, with the corresponding numerical values listed in the top part of Table 2 (designated as the "APOGEE instrument"). The most notable feature seen in Figure 6 is a "tail" of models in the T_{eff} range between some 8000 K and 10,000 K in the top-left panel, where we record about 25 of the ZETA-PAYNE best-fit models that show T_{eff} discrepancies of above some 600 K and up to some 2500 K with the true values. The discrepancy is confined to that specific $\sim$2000 K wide T_{eff} interval and occurs in the low [M/H] to high $v \sin i$ range of the parameter space. As demonstrated in the top-left panel in Figure 7, the APOGEE spectra are dominated by the Brackett series of hydrogen lines having very low sensitivity to the T_{eff} variations in that particular T_{eff} interval. Therefore, metal lines represent an important T_{eff} diagnostic. However, the cumulative effect of low metallicity and high projected rotational velocity of the star makes metal lines appear weak and shallow. Altogether, the overly weak metal lines and low sensitivity of the Brackett series to T_{eff} variations act as a source of confusion (hence large internal uncertainty) for the spectrum analysis algorithm in the T_{eff} bin under consideration. The degeneracy gets progressively smaller with increasing metallicity (and decreasing projected rotational velocity), so that the internal uncertainty in T_{eff} becomes comparable to adjacent T_{eff} bins as [M/H] approaches the solar value (see the bottom-left panel in Figure 7 where the growth of the strength of metal lines
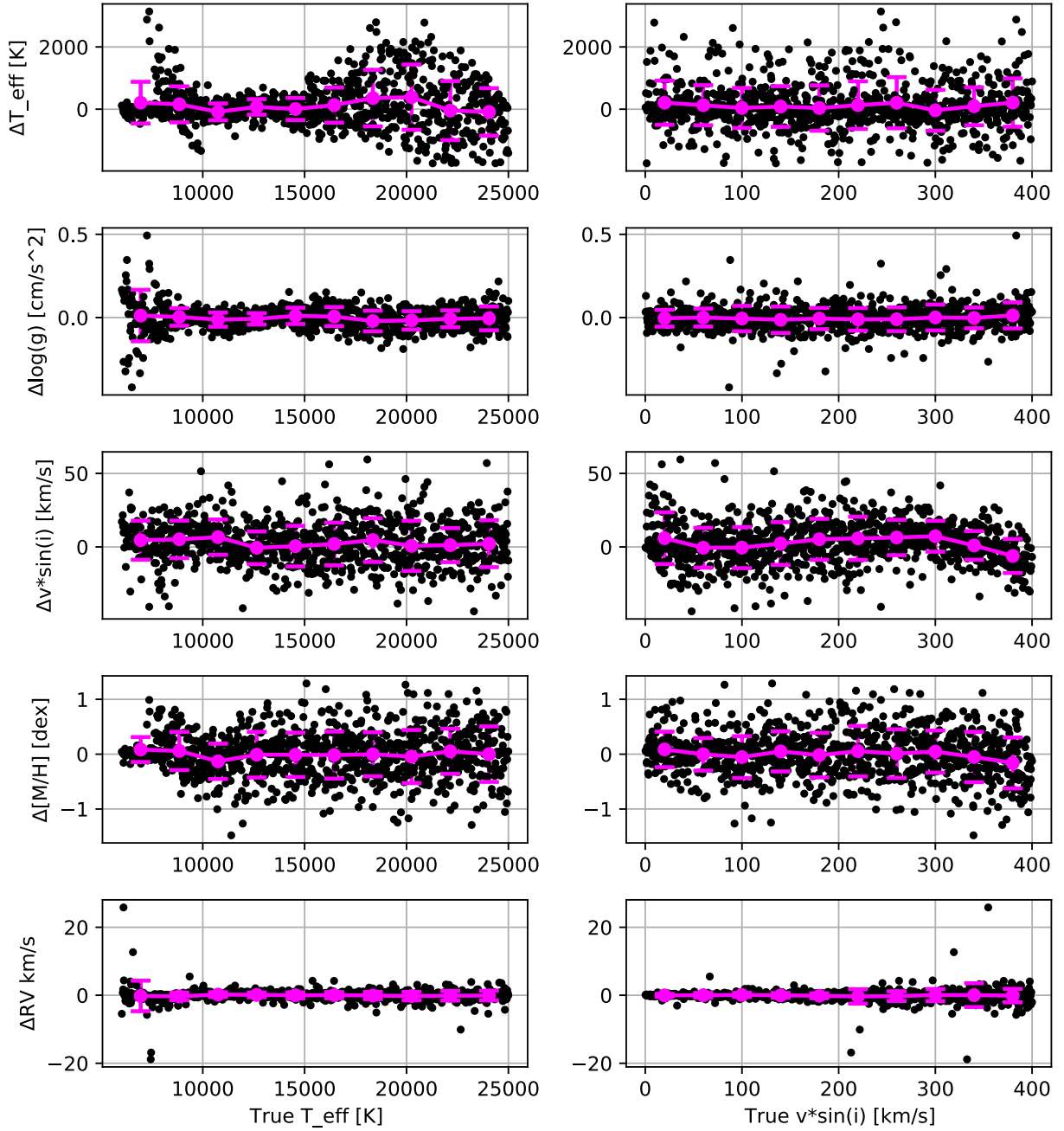
Figure 6. Differences between the parameters inferred with the ZETA-PAYNE algorithm from the simulated noiseless APOGEE spectra and their true values (black dots), as a function of the true $T_{\rm eff}$ (left) and $v \sin i$ (right). From top to bottom: the differences are shown for $T_{\rm eff}$, $\log g$, $v \sin i$, [M/H], and radial velocity (RV). The internal uncertainties per parameter bin are shown with the magenta full circles with error bars; definitions of the individual parameter bins is given in Table 2.

compared to the low [M/H] case is visible). We also note a larger internal uncertainty in the effective temperature of the star at $T_{\rm eff} \gtrsim 15{,}000$ K (top-left panel in Figure 6) that we attribute to the fact that the APOGEE spectra of late O- and B-type stars are largely featureless and dominated by the Brackett series of broad hydrogen lines. The spectra additionally suffer from two wavelength gaps present in the APOGEE data that reduce the amount of available information and thus contribute to the internal uncertainty. A lower internal uncertainty in the metallicity of the star is also seen in the low $T_{\rm eff}$ ($\lesssim 8000$ K) and low $v \sin i$ ($\lesssim 40$ km s^{-1}) region of the parameter space (see penultimate panel in the left column in Figure 6). This result can be explained by the larger number of (narrow) metal lines available in those spectra for the inference

of stellar metallicity, while the lines either disappear or get significantly broadened at higher effective temperatures and projected rotational velocities, respectively.

Table 3 (left column, designated as "APOGEE") lists the internal uncertainties for all five stellar parameters ($T_{\rm eff}$, $\log g$, $v \sin i$, [M/H], and radial velocity, RV) as inferred from the entire simulated APOGEE data set, which makes them representative of the parameter space in consideration. We also note that a similar exercise was performed for the simulated APOGEE data sets characterized by S/N = 50 and 100 as an indication of the effect of Poisson noise on the resulting internal uncertainties. The results are summarized in the APOGEE instrument "S/N = 50" and "S/N = 100" columns in Table 3. One can see that overall uncertainty in

Table 2

RMS Errors (Internal Uncertainty) per Bin for the Stellar Parameters Recovered by the Developed ZETA-PAYNE Algorithm from Simulated Noiseless APOGEE and BOSS Spectra (Mimicking Infinite S/N Value)

Parameter	Internal Uncertainty (rms)									
	Bin 1	Bin 2	Bin 3	Bin 4	Bin 5	Bin 6	Bin 7	Bin 8	Bin 9	Bin 10
APOGEE instrument as a function of $T_{\rm eff}$										
Bin, kK	6-7.9	7.9–9.8	9.8–11.7	11.7–13.6	13.6–15.5	15.5–17.4	17.4–19.3	19.3–21.2	21.2–23.1	23.1–25
$T_{\rm eff}$, K	670	579	269	249	354	563	908	1048	949	764
$\log g$, dex	0.15	0.05	0.04	0.03	0.05	0.06	0.06	0.06	0.05	0.07
$v \sin i$, km s^{-1}	13	13	12	11	14	15	15	17	12	16
[M/H], dex	0.23	0.35	0.32	0.42	0.40	0.43	0.40	0.49	0.41	0.51
RV, km s^{-1}	4.5	1.1	0.7	0.7	0.9	0.9	1.1	1.2	1.4	1.4
as a function of $v \sin i$										
Bin, km s^{-1}	0–40	40–80	80–120	120–160	160–200	200–240	240–280	280–320	320–360	360–400
$T_{\rm eff}$, K	709	643	644	653	728	764	821	657	609	776
$\log g$, dex	0.05	0.05	0.08	0.08	0.06	0.07	0.07	0.08	0.06	0.08
$v \sin i$, km s^{-1}	18	14	14	15	14	15	12	11	10	12
[M/H], dex	0.32	0.30	0.38	0.37	0.41	0.46	0.44	0.38	0.46	0.46
RV, km s^{-1}	0.4	0.7	0.6	0.7	0.7	2.1	1.4	1.8	3.5	2.0
BOSS instrument as a function of $T_{\rm eff}$										
Bin, kK	6–7.9	7.9–9.8	9.8–11.7	11.7–13.6	13.6–15.5	15.5–17.4	17.4–19.3	19.3–21.2	21.2–23.1	23.1–25
$T_{\rm eff}$, K	50	80	96	83	98	146	197	209	222	268
$\log g$, dex	0.09	0.06	0.04	0.02	0.02	0.02	0.02	0.02	0.02	0.04
$v \sin i$, km s^{-1}	19	16	15	11	11	13	12	10	11	15
[M/H], dex	0.06	0.11	0.11	0.07	0.11	0.08	0.09	0.09	0.08	0.12
RV, km s^{-1}	1.1	1.2	0.5	0.4	0.2	0.2	0.4	0.4	0.3	0.7
as a function of $v \sin i$										
Bin, km s^{-1}	0–40	40–80	80–120	120–160	160–200	200–240	240–280	280–320	320–360	360–400
$T_{\rm eff}$, K	174	144	158	166	157	149	152	175	159	180
$\log g$, dex	0.03	0.04	0.04	0.05	0.04	0.04	0.04	0.05	0.04	0.06
$v \sin i$, km s^{-1}	19	16	15	16	8	9	9	10	9	10
[M/H], dex	0.08	0.08	0.08	0.11	0.07	0.08	0.09	0.13	0.09	0.11
RV, km s^{-1}	0.3	0.4	0.3	0.4	0.6	0.5	0.7	1.0	0.7	1.0

Note. The uncertainties are reported for both instruments and as a function of $T_{\rm eff}$ and $v \sin i$ of the spectrum.

$T_{\rm eff}$ and $v \sin i$ increases by some 15% and 50%, respectively, between the noiseless and S/N = 50 spectra, while there is hardly any change in the uncertainty for $\log g$ of the star. The largest increase by a factor of ~5 is recorded for the uncertainty in the RV of the star (1.25 km s^{-1} in the noiseless case as compared to 6.27 km s^{-1} for S/N = 50), while the increase of some 0.1 dex is observed for the uncertainty in stellar metallicity.

The above-described approach is also applied to the BOSS simulated spectra; the results obtained for the noiseless data set are presented in Figure 8 and in Tables 2 and 3. In addition to the expected increase in the internal uncertainty for $T_{\rm eff}$ of the star toward higher effective temperatures (top panel in the left column in Figure 8), a larger scatter is also recorded for $\log g$ of the star at $T_{\rm eff}$ values below some 10,000 K (second top panel in the left column in Figure 8). This effect is explained by low sensitivity of the merit function employed in the optimization algorithm to $\log g$ variations in the $T_{\rm eff}$ range of late A- to F-type stars. Indeed, as discussed in detail, e.g., in (Gebruers et al. 2021, see their Section 4.1), metal lines along with the central cores of the Balmer lines represent the main diagnostic for the inference of the surface gravity of these stars

at optical wavelengths. Owing to the low spectral resolution of the BOSS instrument, the number of spectral bins that appear to be sensitive to $\log g$ variations is small relative to the total number of bins that contribute to the merit function. Coupled with partial degeneracy between the $\log g$ and $T_{\rm eff}$ parameters in the spectroscopic analysis of intermediate spectral type stars, this results in larger internal uncertainty for $\log g$ in the $T_{\rm eff}$ regime of late A- to F-type stars. Finally, we observe an increase of the uncertainty for $T_{\rm eff}$ and $v \sin i$ of the star by some 25% and 15%, respectively, when degrading the quality of input data from the noiseless case to S/N of 50. An increase by a factor of ~2 is also observed for the RV uncertainty, while the uncertainties for $\log g$ and [M/H] remain largely unchanged (see Table 3).

5. Application of ZETA-PAYNE to Control Stellar Samples

Aside from the successful performance test on simulated spectra discussed in Section 4, we apply the ZETA-PAYNE algorithm to spectra of two control samples of real stars. First, we employ the sample of slowly pulsating B-type (SPB) stars analyzed in Gebruers et al. (2021) to test if we can reproduce
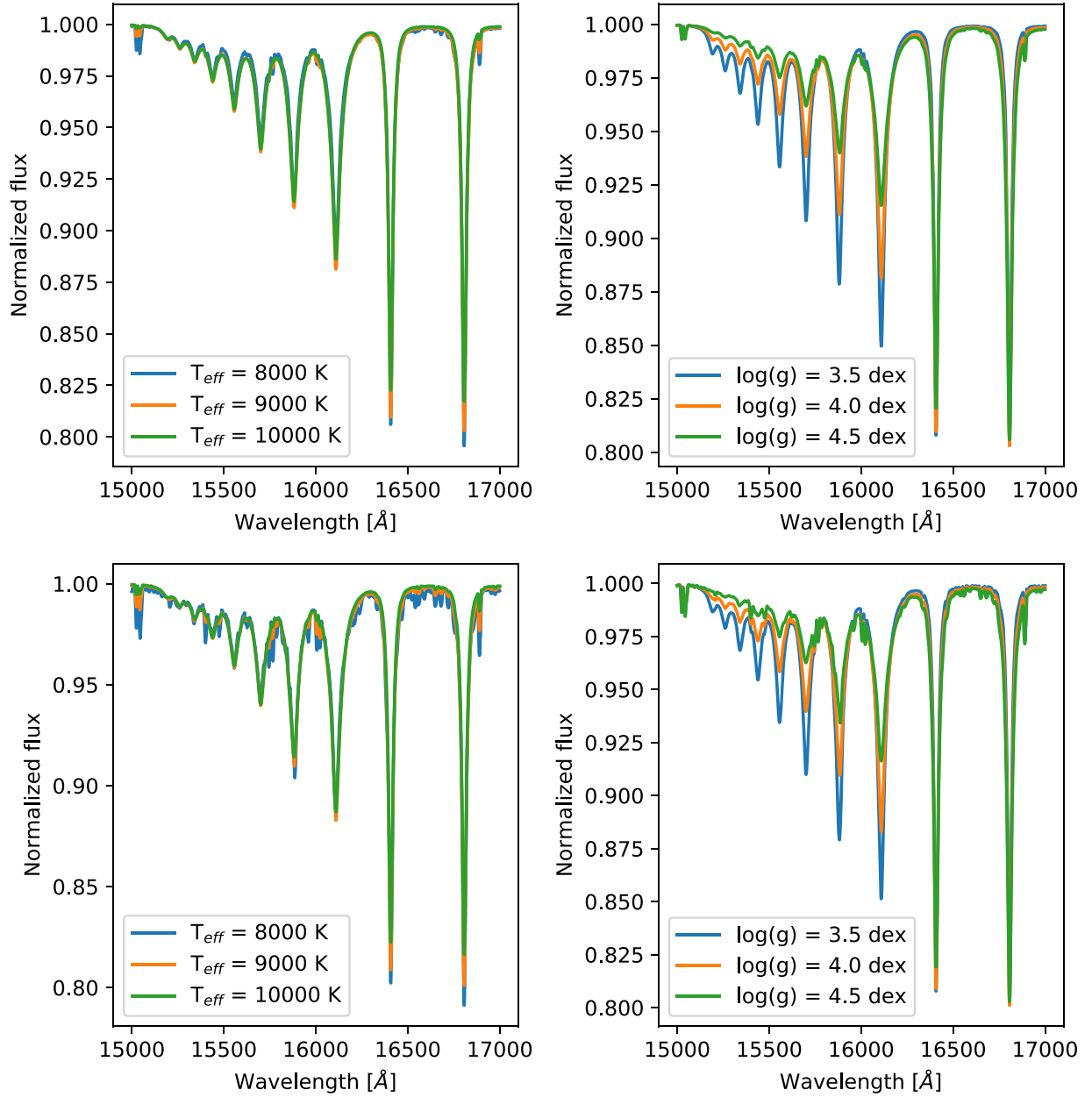
Figure 7. Effect of the $T_{\rm eff}$ and log g parameter changes on the appearance of stellar spectra of late A- to early F-type stars in the wavelength range of the APOGEE instrument. The top and bottom rows show the effect at significantly subsolar ([M/H] = −0.8 dex) and solar ([M/H] = 0.0 dex) metallicity, respectively. Left column: blue, orange, and green lines represent models with $T_{\rm eff}$ = 8000, 9000, and 10,000 K, respectively; log g and $v \sin i$ are kept fixed at 4.0 dex and 150 km s^{-1}, respectively. Right column: blue, orange, and green lines represent models with log g = 3.5, 4.0, and 4.5 dex, respectively; $T_{\rm eff}$ and $v \sin i$ are kept fixed at 9000 K and 150 km s^{-1}, respectively.

Table 3
Root Mean Square Errors (Internal Uncertainty) Averaged over the Entire Parameter Space for the Stellar Parameters as Inferred from the Simulated APOGEE and BOSS Spectra with Realistic Noise Levels

| | Internal Uncertainty (rms) | | | | | |
| Parameter | APOGEE | | | BOSS | | |
	Noiseless	S/N = 100	S/N = 50	Noiseless	S/N = 100	S/N = 50
$T_{\rm eff}$, K	707	736	791	163	177	206
log g, dex	0.07	0.08	0.09	0.043	0.044	0.045
$v \sin i$, km s^{-1}	14	17	23	14	15	16
[M/H], dex	0.41	0.46	0.50	0.10	0.10	0.11
RV, km s^{-1}	1.67	3.65	6.30	0.65	1.29	2.19
Reliability	96.2%	96.5%	95.6%	95.6%	97.4%	97.3%
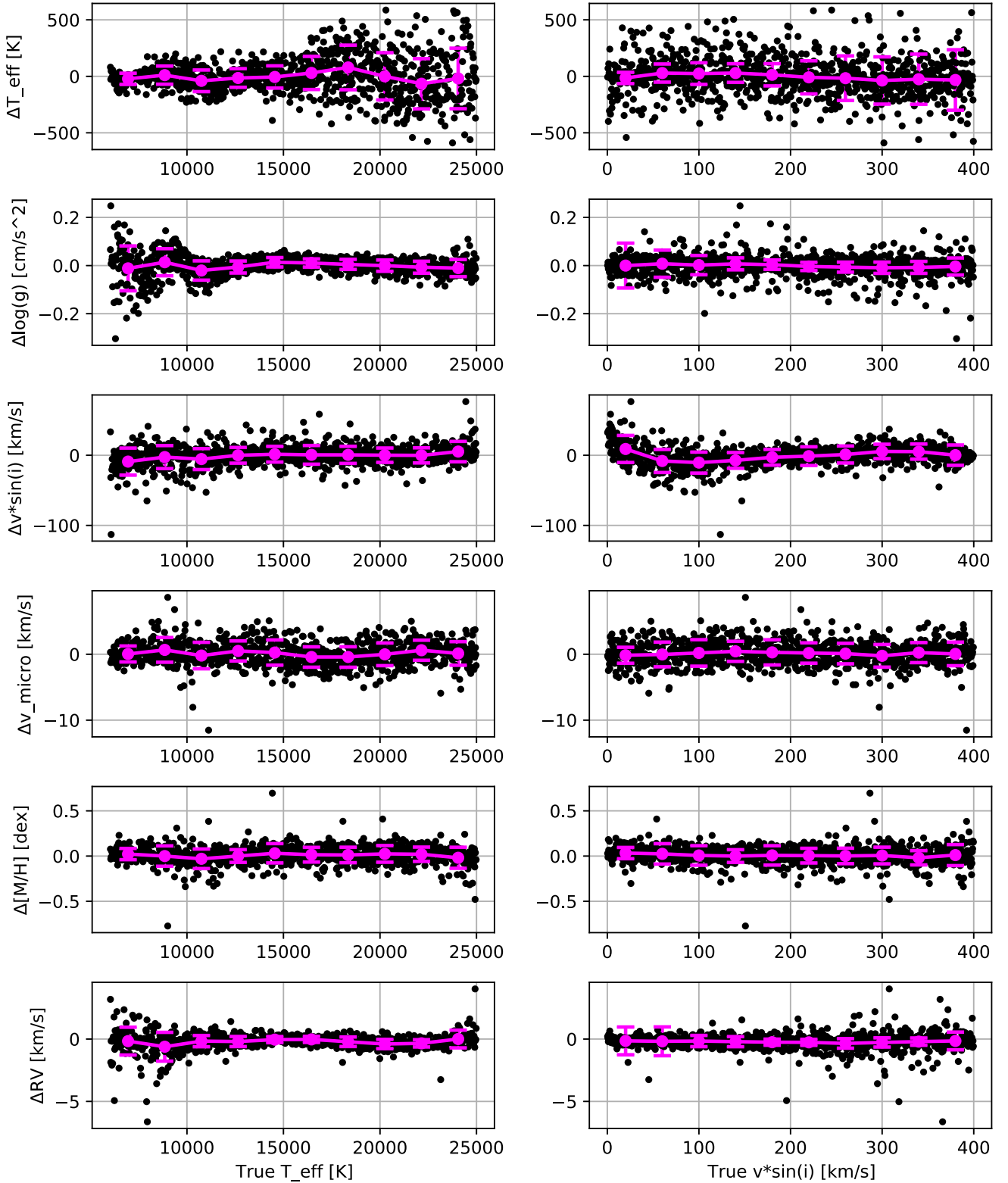
Figure 8. The same as Figure 6 but for the simulated noiseless BOSS data.

their results with respect to the atmospheric parameters of the stars inferred from both high-resolution ($R \approx 85{,}000$) HERMES (Raskin et al. 2011) and low-resolution ($R \approx 1800$) LAMOST optical spectra. At the time of writing, we do not have any OBAF-type stars observed with the BOSS instrument in SDSS-V that would be bright enough for observations with the HERMES instrument at the 1.2 m Mercator telescope and

with the APOGEE instrument (see below). Therefore, we decide to use LAMOST spectra instead, given a number of similarities with the BOSS instrument, among which are the wavelength coverage, resolving power, and spectrum reduction pipelines. This exercise allows us to quantify potential differences in the inferred stellar parameters with respect to those derived in Gebruers et al. (2021), as well as to unravel
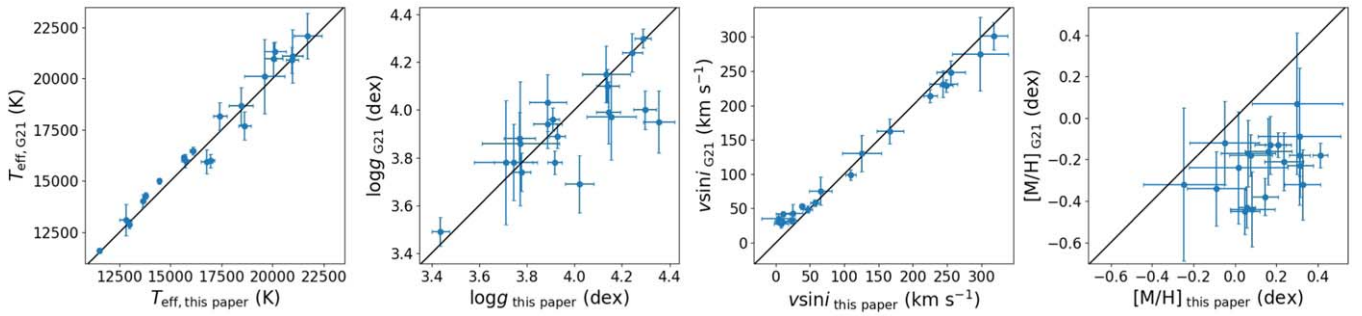
Figure 9. Comparison between stellar parameters of 20 Kepler SPB-type stars as inferred from their high-resolution optical spectra in Gebruers et al. (2021) and in this study. From left to right: T_{eff}, $\log g$, $v \sin i$, and [M/H]. The solid black line indicates the one-to-one correspondence between the parameters and is shown to help guide the eye. The shown error bars reflect 1σ statistical uncertainties and do not include the internal uncertainty reported in Section 4.

potential systematic effects in the inferred atmospheric parameters associated with a factor of ∼40 reduction in the spectral resolution (HERMES versus LAMOST). Second, we cross-match a sample of OBAF-type star candidates observed with the APOGEE instrument as part of the SDSS-V Pathfinder program (Kollmeier et al. 2017) with archival HERMES high-resolution optical observations, and analyze both data sets with the ZETA-PAYNE algorithm. These tests offer a cross-validation between the parameter inference from medium-resolution near-IR and high-resolution optical spectra. When combined with the results of the previous exercise based on the sample of Gebruers et al. (2021), this also allows us to close the loop of cross-validation between the SDSS-V APOGEE and BOSS instruments and high-resolution optical spectroscopy of OBAF-type stars that cannot be assembled for the large SDSS-V sample.

Gebruers et al. (2021) used an earlier version of the ZETA-PAYNE algorithm to analyze a sample of 111 pulsating B- and F-type stars in the Kepler field based on high-resolution ($R = 85,000$) optical HERMES spectra. Two important differences between the version of the ZETA-PAYNE algorithm presented in this study and the version used in Gebruers et al. (2021) are that the latter study: (1) used a training scheme only based on a quasi-random sampling of the training examples after Sobol (1967), and (2) included the microturbulent velocity as a free parameter in view of the high resolution of the spectra used in their analysis. Difference (1) has important consequences for slowly rotating stars where extra care has to be taken during the training process to fully capture the rapidly increasing morphological complexity of stellar spectra compared to the cases of moderate to high projected rotational velocities (Section 3.2). The inclusion of the microturbulent velocity as a free parameter is expected to result in a notable difference in the inferred stellar metallicity because of nonnegligible correlations between those two parameters.

Figure 9 shows a comparison between the T_{eff}, $\log g$, $v \sin i$, and [M/H] parameters as inferred from the HERMES high-resolution spectra in Gebruers et al. (2021) and in this study (see also Table 4 for numerical values; columns designated as "HERMES"). We observe a good agreement within the quoted 1σ statistical uncertainties (i.e., not taking the internal uncertainty into account) for T_{eff} of the star, for $\log g$, and $v \sin i$ for most part of the sample. However, [M/H] derived here is systematically higher than the corresponding values obtained in Gebruers et al. (2021). The small but statistically significant discrepancy observed for $v \sin i$ for the slowest rotators in the sample is explained by a more sophisticated and

precise training of the neural network performed in this study in the corresponding region of the parameters space, as discussed in detail in Section 3.2. There are also five objects for which we find systematically larger $\log g$ values than reported in Gebruers et al. (2021; see second panel in Figure 9). Those are the five slowest rotators in the sample for which we also find discrepant values of the projected rotational velocity compared with Gebruers et al. (2021) due to their suboptimal training of the neural network. The systematic offset in the derived metallicity of the stars is associated with our exclusion of the microturbulent velocity ξ from the free parameter vector as we kept it fixed to $2.0 \, km \, s^{-1}$. Indeed, as demonstrated in Figure 10, the depths of most of the spectral lines of metals (and to a lesser extent of helium) steadily increase with increasing microturbulent velocity. This way, when synthetic spectra are computed for the $2.0 \, km \, s^{-1}$ fixed value of the microturbulent velocity while the star, in reality, shows a larger value of microturbulence, the spectrum analysis algorithm tends to compensate for the observed difference in the line depths of metals. This is most easily achieved by increasing the [M/H] parameter in the models. The effect is quantitatively demonstrated in Table 5, where we summarize the results of the ZETA-PAYNE analysis of five artificial spectra, each one computed with a different value of the microturbulent velocity parameter (from $2 \, km \, s^{-1}$ to $10 \, km \, s^{-1}$ in steps of $2 \, km \, s^{-1}$) but with fixed values of $T_{eff} = 13,000$ K, $\log g = 4.0$ dex, $v \sin i = 100 \, km \, s^{-1}$, and [M/H] $= 0.0$ dex. One can see that while we successfully recover T_{eff}, $\log g$, and $v \sin i$ from the input spectrum within the quoted 1σ statistical uncertainties in all five test cases, the discrepancy between the inferred and assumed metallicity steadily increases with the microturbulent velocity and reaches some 0.5 dex for the most extreme considered case of $\xi = 10.0 \, km \, s^{-1}$.

We further proceed with the analysis of the LAMOST spectra of exactly the same sample of Kepler SPB-type stars. We note that two out of 20 stars do not have LAMOST spectra; hence, this particular analysis is restricted to 18 stars for which low-resolution spectra could be found in the LAMOST data archive. Our goal here is to quantify the effects of a factor ∼40 reduction in the resolving power of the instrument and substantially different properties of its response function on the inferred atmospheric parameters of the star. The results of our analysis are summarized in Figure 11 and Table 4 (columns designated as "LAMOST"). We find an overall good agreement within the quoted 1σ statistical uncertainties between the T_{eff}, $v \sin i$, and [M/H] parameters derived from the HERMES high-resolution and LAMOST low-resolution optical spectra. There

Table 4
Stellar Parameters of the 20 SPB Stars from Gebruers et al. ([2021](#)) as Inferred in This Study from Their HERMES High-resolution and LAMOST Low-resolution Optical Spectra (Two of These Stars Only Have HERMES Spectra)

KIC Number	$T_{\rm eff}$ (K)		$\log g$ (dex)		$v \sin i$ (km s^{-1})		[M/H] (dex)	
	HERMES	LAMOST	HERMES	LAMOST	HERMES	LAMOST	HERMES	LAMOST
10285114	15994 ± 262	16429 ± 649	4.04 ± 0.05	4.09 ± 0.13	247 ± 24	236 ± 72	-0.04 ± 0.11	-0.21 ± 0.34
10536147	21225 ± 711	21013 ± 1126	3.81 ± 0.09	3.71 ± 0.14	174 ± 17	139 ± 47	-0.20 ± 0.13	-0.08 ± 0.20
11360704	17856 ± 398	17608 ± 957	3.91 ± 0.06	3.90 ± 0.13	307 ± 26	301 ± 64	-0.12 ± 0.13	-0.16 ± 0.35
12258330	16320 ± 149	16432 ± 601	4.27 ± 0.04	4.12 ± 0.13	118 ± 7	78 ± 66	-0.10 ± 0.06	-0.37 ± 0.29
3240411	21985 ± 300	20708 ± 1014	4.22 ± 0.05	4.09 ± 0.14	36 ± 4	31 ± 65	-0.12 ± 0.04	0.01 ± 0.17
3756031	17302 ± 297	16925 ± 659	3.95 ± 0.06	3.90 ± 0.12	14 ± 6	21 ± 39	-0.35 ± 0.12	-0.33 ± 0.43
3839930	17436 ± 239	17237 ± 660	4.32 ± 0.05	4.34 ± 0.13	28 ± 6	30 ± 61	0.02 ± 0.07	-0.27 ± 0.35
3865742	19776 ± 1242	19941 ± 1210	3.89 ± 0.16	3.82 ± 0.16	132 ± 40	110 ± 65	0.27 ± 0.19	0.03 ± 0.22
5941844	14105 ± 141	13806 ± 445	4.33 ± 0.04	4.26 ± 0.13	28 ± 3	24 ± 98	0.05 ± 0.06	0.10 ± 0.32
6462033	18171 ± 537	18645 ± 772	4.22 ± 0.11	4.17 ± 0.13	73 ± 18	28 ± 103	-0.08 ± 0.18	-0.60 ± 0.45
6780397	13150 ± 141	13068 ± 373	3.77 ± 0.04	3.63 ± 0.10	57 ± 6	61 ± 53	-0.07 ± 0.06	-0.19 ± 0.26
7760680	11570 ± 97	11858 ± 209	3.91 ± 0.03	4.22 ± 0.08	72 ± 6	0 ± 30	0.18 ± 0.08	-0.02 ± 0.27
8057661	23795 ± 661	21693 ± 1219	4.40 ± 0.12	4.52 ± 0.17	33 ± 9	33 ± 77	-0.22 ± 0.09	-0.14 ± 0.24
8087269	13198 ± 471	13043 ± 421	3.73 ± 0.12	3.59 ± 0.10	287 ± 83	257 ± 78	0.11 ± 0.23	-0.21 ± 0.41
8381949	21288 ± 517	22300 ± 1148	3.93 ± 0.07	4.23 ± 0.13	220 ± 19	206 ± 60	-0.10 ± 0.10	-0.34 ± 0.42
8714886	19148 ± 623	18430 ± 675	4.24 ± 0.07	4.44 ± 0.13	19 ± 7	35 ± 38	-0.05 ± 0.09	-0.17 ± 0.30
8766405	14498 ± 156	14427 ± 680	3.49 ± 0.03	3.22 ± 0.14	209 ± 14	227 ± 70	-0.27 ± 0.08	-0.63 ± 0.44
9964614	21387 ± 532	21049 ± 1033	4.00 ± 0.08	4.22 ± 0.14	46 ± 10	1 ± 57	-0.20 ± 0.10	-0.34 ± 0.27
11971405	15084 ± 136	$\cdots$	3.89 ± 0.03	$\cdots$	223 ± 13	$\cdots$	-0.10 ± 0.06	$\cdots$
8459899	16311 ± 135	$\cdots$	3.89 ± 0.03	$\cdots$	47 ± 4	$\cdots$	0.00 ± 0.05	$\cdots$

Note. The quoted parameter uncertainties reflect 1σ statistical uncertainties and do not account for the internal uncertainties reported in Section [4](#).
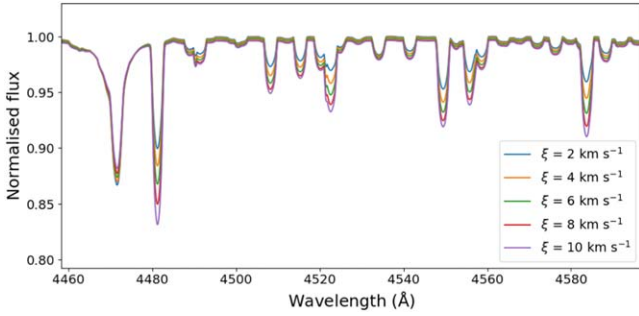
Figure 10. Synthetic spectra computed for $T_{\rm eff} = 13{,}000$ K, $\log g = 4.0$ dex, $v \sin i = 100$ km s^{-1}, and [M/H] $= 0.0$ dex and varying microturbulent velocity ξ from 2 to 10 km s^{-1}.

Table 5
Parameters Inferred with the ZETA-PAYNE Algorithm from the Input Artificial Spectra That Assume $T_{\rm eff}$, $\log g$, $v \sin i$, and [M/H] Fixed to 13,000 K, 4.0 dex, 100 km s^{-1}, and 0.0 dex, Respectively, and Variable Microturbulent Velocity ξ Parameter as Indicated in the First Column

Input Spectrum	Inferred Parameters			
ξ (km s^{-1})	$T_{\rm eff}$ (K)	$\log g$ (dex)	$v \sin i$ (km s^{-1})	[M/H] (dex)
2	$13\,110 \pm 22$	4.01 ± 0.01	94 ± 3	$+0.02 \pm 0.02$
4	$13\,109 \pm 31$	4.02 ± 0.01	95 ± 4	$+0.15 \pm 0.03$
6	$13\,057 \pm 45$	4.03 ± 0.02	99 ± 8	$+0.29 \pm 0.03$
8	$13\,039 \pm 52$	4.05 ± 0.03	95 ± 4	$+0.42 \pm 0.03$
10	$13\,014 \pm 62$	4.04 ± 0.03	95 ± 5	$+0.49 \pm 0.04$

Note. The quoted parameter errors are 1σ statistical uncertainties.

is a small population of stars whose $\log g$ values as inferred from the LAMOST spectra exceed those derived from the HERMES high-resolution spectra, where the agreement occurs only at 2σ instead of 1σ statistical uncertainty level (see the top-right panel in Figure [11](#)). These discrepant cases are located in the region of high surface gravity, i.e., $\log g \gtrsim 3.9$ dex, and are in agreement with each other when internal uncertainties are also taken into account.

Finally, the ZETA-PAYNE algorithm is applied to a sample of B- to F-type stars that were observed with the APOGEE instrument as part of the SDSS-V Pathfinder program in the northern hemisphere and for which high-resolution optical spectra exist in the HERMES data archive. The results of our analysis are illustrated in Figure [12](#) and summarized in Table [6](#). As expected, the $v \sin i$ parameter can realistically be inferred from the APOGEE spectra for the coolest and slowly rotating F-type stars only, owing to a large number of strong metal lines found in the spectra of these objects. For the rest of the sample, the APOGEE spectra are dominated by the broad hydrogen lines of the Brackett series, which results in significant and systematic overestimation of the projected rotational velocity of the star compared to the case of high-resolution optical spectra. Similarly, we observe a significant discrepancy between the surface gravity $\log g$ values inferred from the APOGEE and from the high-resolution optical spectra, with no clear dependency on $T_{\rm eff}$ or $v \sin i$ of the star. The observed discrepancy is the result of a degeneracy between the surface gravity of the star and parameters of the residual response function model in the analysis of the near-IR APOGEE spectra. Indeed, as illustrated in Figure [7](#) (right column), the wavelength region in the APOGEE spectra between some 1.5 μm and 1.6 μm (where the density of hydrogen lines steadily increases and they ultimately merge) is the most informative one for the inference of the surface gravity of B- to F-type stars. However, that particular part of the spectrum is also the most uncertain one in fitting the residual response function, leading to the above-mentioned degeneracy. Finally, we find a reasonably good agreement between the $T_{\rm eff}$ values inferred from the near-IR APOGEE and high-resolution optical spectra, with a small
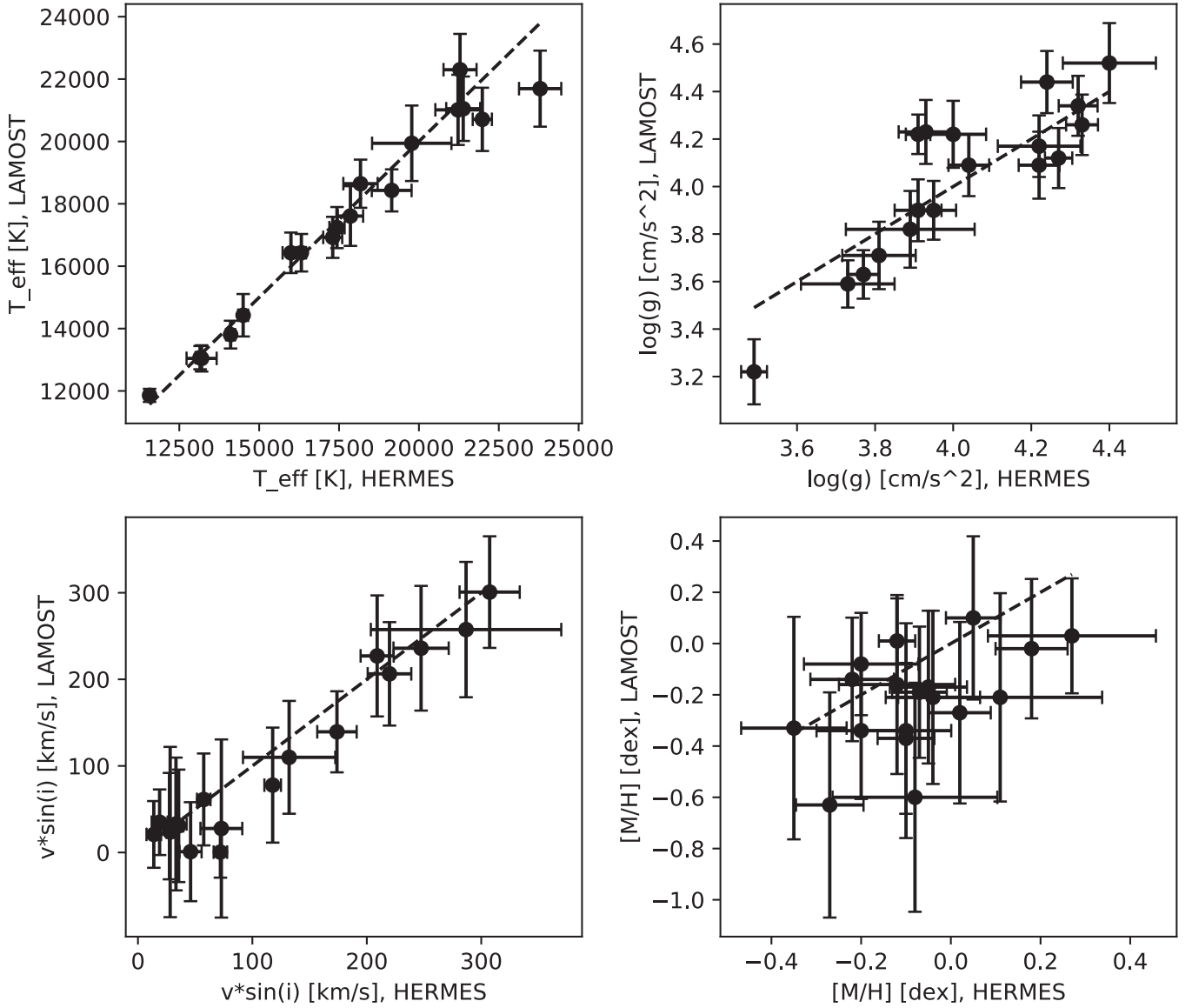
Figure 11. Comparison between stellar parameters inferred with the ZETA-PAYNE algorithm from the HERMES high-resolution and LAMOST low-resolution optical spectra of a sample of 18 SPB stars from Gebruers et al. (2021). The dashed black line indicates the one-to-one correspondence between the parameters and is shown to help guide the eye. The error bars reflect 1σ statistical uncertainties of the fit and do not account for the internal parameter uncertainties.
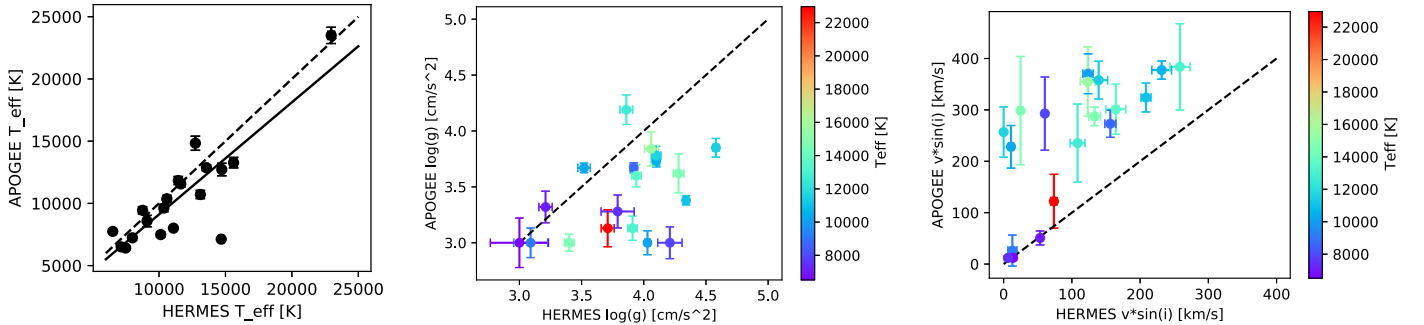
Figure 12. Comparison between atmospheric parameters derived from the medium-resolution near-IR APOGEE and high-resolution optical HERMES spectra. From left to right: $T_{\rm eff}$, $\log g$, and [M/H] of the star. The dashed and solid lines represent the one-to-one correspondence and the best-fit linear regression model, respectively. The error bars shown reflect 1σ statistical uncertainties of the fit. See the text for details.

but statistically significant underestimation of the effective temperature of the star from the near-IR spectra. The linear regression analysis gives an intercept and slope of 104 K and 0.9, respectively, with the null hypothesis of equal values being

rejected at the level of a p-value of 2.3×10^{-6} (see also the left panel in Figure 12). We interpret the observed difference in the inferred $T_{\rm eff}$ parameter as being due to the cumulative effect of (i) a much more limited amount of information in the near-IR

Table 6
Stellar Parameters of 19 B- to F-type Stars as Derived in This Study from Their APOGEE Medium-resolution Near-IR and HERMES High-resolution Optical Spectra

Star Name	$T_{\rm eff}$ (K)		$\log g$ (dex)		$v \sin i$ (km s^{-1})	
	HERMES	APOGEE	HERMES	APOGEE	HERMES	APOGEE
16371249+7609490	7493 ± 50	6413 ± 140	3.79 ± 0.13	3.28 ± 0.15	6 ± 1	12 ± 4
16462193+7701175	15611 ± 250	13274 ± 424	4.06 ± 0.05	3.84 ± 0.15	123 ± 11	355 ± 68
16472272+6905558	11085 ± 35	8008 ± 75	4.34 ± 0.02	3.38 ± 0.04	209 ± 7	324 ± 28
16524392+7651096	7152 ± 21	6506 ± 142	3.21 ± 0.05	3.32 ± 0.14	53 ± 1	51 ± 14
17033403+5729591	11449 ± 57	11836 ± 329	4.58 ± 0.02	3.85 ± 0.08	139 ± 13	358 ± 37
17122286+5713243	10358 ± 93	9625 ± 298	3.52 ± 0.05	3.67 ± 0.04	11 ± 4	228 ± 41
17264168+5944556	14724 ± 146	12722 ± 507	4.28 ± 0.04	3.62 ± 0.17	25 ± 4	299 ± 105
17503133+5726367	10590 ± 51	10372 ± 271	4.10 ± 0.02	3.73 ± 0.05	232 ± 14	377 ± 18
18132623+6445575	13569 ± 141	12864 ± 240	3.94 ± 0.04	3.60 ± 0.10	164 ± 15	301 ± 49
18440460+6046128	9095 ± 186	8578 ± 463	3.09 ± 0.14	3.00 ± 0.13	13 ± 7	26 ± 30
18520222+5940014	13110 ± 127	10713 ± 333	3.91 ± 0.04	3.13 ± 0.11	258 ± 15	384 ± 84
18534470+6001044	14680 ± 159	7124 ± 89	3.40 ± 0.04	3.00 ± 0.08	133 ± 9	287 ± 18
18585261+6931525	12736 ± 132	14837 ± 568	3.86 ± 0.05	4.19 ± 0.13	108 ± 11	235 ± 76
19094260+6451320	6518 ± 38	7747 ± 102	3.00 ± 0.23	3.00 ± 0.22	14 ± 1	12 ± 5
19162421+6708066	22956 ± 256	23502 ± 657	3.71 ± 0.05	3.13 ± 0.17	74 ± 5	122 ± 52
19181164+6057360	11633 ± 74	11563 ± 248	4.10 ± 0.04	3.78 ± 0.08	0 ± 1	257 ± 49
19224444+7438013	8760 ± 40	9442 ± 291	3.92 ± 0.03	3.67 ± 0.05	156 ± 8	273 ± 26
19373625+6401001	7994 ± 36	7232 ± 210	4.21 ± 0.10	3.00 ± 0.14	60 ± 3	293 ± 71
20000399+6826121	10127 ± 47	7490 ± 214	4.03 ± 0.02	3.00 ± 0.11	124 ± 8	370 ± 39

Note. The analysis assumes a fixed metallicity [M/H] = 0.0 dex. The quoted parameter uncertainties reflect 1σ statistical uncertainties and do not account for the internal uncertainties reported in Section 4. See the text for details.

spectra of B- to F-type stars as compared to the optical wavelengths, (ii) partial methodological degeneracy between $T_{\rm eff}$, $\log g$, and parameters of the residual response function model, and (iii) physical effects like different sensitivity of spectral lines of hydrogen and metals to non-LTE effects at the optical and near-IR wavelengths. We also note that the above-described analysis was performed assuming a fixed value of the stellar metallicity [M/H] = 0.0 dex because of the lack of information for the inference of the respective parameter from the near-IR spectra and the associated large internal uncertainty (see Figure 6 and Table 3).

6. Conclusions and Future Prospects

In this study, we develop a fully automated, ML-based spectrum analysis algorithm ZETA-PAYNE, whose main purpose is to serve the MWM program of the SDSS-V survey in its daily data analysis routine. Though the algorithm is mainly positioned for the analysis of intermediate- to high-mass stars of spectral types O, B, A, and F, it can easily be extended toward lower stellar effective temperatures and masses, if necessary. This paper presents a detailed description of the spectrum analysis algorithm and the statistical framework it is embedded in. It details the algorithm training, validation, and testing steps. The algorithm tests are performed both on artificial medium-resolution near-IR and low-resolution optical spectra, and on two control samples of real stars for which (HERMES) high- and (LAMOST) low-resolution optical and (APOGEE) medium-resolution near-IR spectra have been acquired. The main results and conclusions of the paper are as follows:

1. The ZETA-PAYNE algorithm is purposely generalized to cover data analysis needs of the MWM program that builds on observations with two multiobject instruments operating in different wavelength regimes and at different resolving powers. To make the algorithm readily applicable to both types of data, where APOGEE spectra of OBAF-type stars in particular suffer from the lack of a well-defined pseudo-continuum, we integrate the spectrum normalization step into the analysis framework where the pseudo-continuum of the star is represented by a series of Chebyshev polynomials. Coefficients of the polynomials are optimized along with atmospheric parameters of the star, thus presenting a valuable alternative to the conventional approach where the input spectrum is (pre-)normalized to the local continuum prior to its detailed analysis.

2. For the algorithm training, we employ a mixture of a quasi-random sampling (Sobol 1967) in the entire parameter space and an additional random grid sampled from a Gaussian distribution at low effective temperatures ($T_{\rm eff} \lesssim 10,000$ K) and projected rotational velocities ($v \sin i \lesssim 30$ km s^{-1}). This hybrid training approach allows us to maximally capture the large diversity in the morphological complexity of stellar spectra when transitioning from hotter and more rapidly rotating B- and A-type stars to cooler F-type objects whose spectra are typically characterized by more narrow metal lines that are also available in numbers.

3. The ZETA-PAYNE algorithm testing on artificial APOGEE medium-resolution near-IR and BOSS low-resolution optical spectra reveals a similar performance at the ~96% level in terms of the reliability metric (defined as the probability that the optimization algorithm converges to a correct set of atmospheric parameters; see Section 4). However, significantly different internal uncertainties occur for the two wavelength regimes. This overall internal uncertainty is lower in the low-resolution optical spectra than in the APOGEE spectra at S/N values of 100 and 50 by a factor of ~3–4 for $T_{\rm eff}$ and RV of the star, and some 0.05 dex and 0.35 dex for its $\log g$ and [M/H], respectively. Thus, we conclude that despite

a factor of 10 lower resolving power of the BOSS instrument compared to the APOGEE spectrograph, optical spectra remain a preferred option for the extraction of atmospheric parameters of OBAF-type stars, unless the latter suffer from high extinction so that their flux can only be observed at longer (e.g., near-IR) wavelengths. We note, however, that this conclusion does not concern inferences of the surface chemical composition of the stars, where resolving individual spectral lines of metals becomes an important factor. The optimal SDSS-V scenario is to observe a star with both the BOSS and APOGEE instruments and rely on the optical and near-IR spectrum for the determination of atmospheric parameters and surface chemical abundances, respectively. An exception would be O- and early B-type stars that do not display spectral lines of metals in the APOGEE spectra (see Figure 1).

4. Application of the ZETA-PAYNE algorithm to the HERMES high-resolution and LAMOST low-resolution optical spectra of 18 objects from the sample of SPB-type stars analyzed spectroscopically in Gebruers et al. (2021) reveals a good agreement between the two sets of atmospheric parameters, including $T_{\rm eff}$, $\log g$, $v \sin i$, and [M/H] of the star. The present version of the ZETA-PAYNE algorithm brings an improved performance in the regime of slowly rotating late A- to F-type stars compared to an earlier version of the algorithm employed in Gebruers et al. (2021). We conclude that as long as the LSF of the instrument is properly accounted for in the analysis of stellar spectra, atmospheric parameters of OBAF-type stars can still be accurately inferred from low-resolution optical spectra, albeit with typically lower precision than from their high-resolution optical spectra. Xiang et al. (2021) came to similar conclusions from the analysis of LAMOST spectra of some 330,000 OBA-type stars and validation of their HOTPAYNE algorithm based on medium- to high-resolution spectra in the literature.

5. Application of the ZETA-PAYNE algorithm to the HERMES high-resolution optical and APOGEE medium-resolution near-IR spectra of a sample of 19 BAF-type stars reinforces our conclusions drawn from the tests with simulated data that the APOGEE near-IR spectra are less suitable for the extraction of accurate atmospheric parameters of OBAF-type stars than optical spectra. Owing to the large dominance of the hydrogen lines of the Brackett series in the APOGEE instrument wavelength range, $v \sin i$ can only be reliably inferred for the coolest F-type stars with slow to moderate rotation. Inference of the stellar surface gravity suffers from strong degeneracy with parameters of the instrument response function model, while the lack of prominent metal lines in the APOGEE spectra of OB (early A)-type stars prevents determination of their atmospheric chemical composition. Finally, the effective temperature of the star is derived with higher accuracy and precision than $v \sin i$ and $\log g$. The intercept and slope of the linear regression model fitted to the difference between $T_{\rm eff}$ inferred from HERMES and APOGEE spectra are 104 K and 0.9, respectively. From the above results, it may appear that there is limited advantage in using the APOGEE spectra for the analysis OBAF-type stars. However, we emphasize that the results based on the APOGEE spectra

obtained with the current version of the ZETA-PAYNE algorithm are still up for improvement owing to the following two assumptions made: (i) the LSF of the instrument is well known and can be described with a wavelength-independent Gaussian kernel corresponding to $R \sim 22{,}500$, and (ii) the residual response function is smooth and sufficiently well-behaved such that it can be approximated with a series of Chebyshev polynomials. None of these assumptions holds in reality, and we need to gain a better understanding of both the APOGEE LSF and residual response function before any firm conclusions can be drawn about the gain of using the near-IR spectra for the analysis of OBAF-type stars.

Although the ZETA-PAYNE pipeline requires little to no human intervention and serves the basic needs of the MWM spectroscopic survey, there is room for improvement. This concerns the input physics currently used in atmospheric models and generalization of the algorithm beyond the analysis of exclusively stellar spectra of single stars. In particular, the (near-)future prospects that we plan for implementation in the forthcoming second release of the ZETA-PAYNE pipeline are:

1. A better understanding and model descriptions of the APOGEE LSF and residual response function.
2. Generalization of the algorithm toward fully automated detection and subsequent analysis of (composite) spectra of spectroscopic double-lined binary stars.
3. Algorithm extension to allow for the determination of surfaces abundances of individual chemical elements such as He, C, N, O, Si, Mg, and Fe.
4. Extension of the currently employed input physics to non-LTE atmospheric models and/or spectral line formation. As discussed in detail in Nieva & Przybilla (2007), the use of the hybrid approach that employs LTE-based atmospheric models and non-LTE spectral line formation is justified for the spectrum analysis of OB-type dwarf and giant stars. Both the hybrid and full non-LTE approaches will be implemented by coupling the TLUSTY (Hubeny & Lanz 1995) non-LTE model atmosphere code to the line formation code currently employed in the ZETA-PAYNE pipeline. For modeling spectra of the hottest and most massive O- and early B-type stars that often have extended atmospheres and winds, we will employ the most recent version of the FASTWIND code (Puls et al. 2005; Sundqvist et al. 2019) to (re-)train the ZETA-PAYNE algorithm in the relevant part of the parameter space.
5. Overall, and for the analysis of APOGEE spectra of OBAF-type stars in particular, it is highly beneficial to include more input options for stellar observables, such as spectral energy distributions and/or photometric colors, and Gaia information. The main purpose of this addition is to provide extra observational constraints, in particular for the effective temperature and surface gravity of the star, to break degeneracies between various parameters in the spectroscopic analysis of OBAF-type stars.

ORCID iDs

Ilya Straumit https://orcid.org/0000-0002-2812-2259
Jeroen Audenaert https://orcid.org/0000-0002-4371-3460
Maosheng Xiang https://orcid.org/0000-0002-5818-8769
Conny Aerts https://orcid.org/0000-0003-1822-7126
Jennifer A. Johnson https://orcid.org/0000-0001-7258-1834
Juna A. Kollmeier https://orcid.org/0000-0001-9852-1610
Hans-Walter Rix https://orcid.org/0000-0003-4996-9069
Rachael L. Beaton https://orcid.org/0000-0002-1691-8217

Jennifer L. Van Saders https://orcid.org/0000-0002-4284-8638
Alexandre Roman-Lopes https://orcid.org/0000-0002-1379-4204
Yuan-Sen Ting https://orcid.org/0000-0001-5082-9536
Carlos G. Román-Zúñiga https://orcid.org/0000-0001-8600-4798

References

Aerts, C. 2021, RvMP, 93, 015001
Aerts, C., Christensen-Dalsgaard, J., & Kurtz, D. W. 2010, Asteroseismology (Berlin: Springer)
Aerts, C., Mathis, S., & Rogers, T. M. 2019, ARA&A, 57, 35
Aerts, C., Molenberghs, G., Michielsen, M., et al. 2018, ApJS, 237, 15
Almeida, L. A., Sana, H., Taylor, W., et al. 2017, A&A, 598, A84
Auvergne, M., Bodin, P., Boisnard, L., et al. 2009, A&A, 506, 411
Banyard, G., Sana, H., Mahy, L., et al. 2022, A&A, 658, A69
Bodensteiner, J., Sana, H., Wang, C., et al. 2021, A&A, 652, A70
Bonifacio, P., Dalton, G., Trager, S., et al. 2016, in SF2A-2016: Proceedings of the Annual meeting of the French Society of Astronomy and Astrophysics, ed. C. Reylé et al. (Lyon: Societe Francaise d'Astronomie et d'Astrophysique), 267
Borucki, W. J., Koch, D., Basri, G., et al. 2010, Sci, 327, 977
Bowen, I. S., & Vaughan, A. H. 1973, ApOpt, 12, 1430
Bowman, D. M., Burssens, S., Pedersen, M. G., et al. 2019, NatAs, 3, 760
Bowman, D. M., Burssens, S., Simón-Díaz, S., et al. 2020, A&A, 640, A36
Branch, M. A., Coleman, T. F., & Li, Y. 1999, SIAM J. Sci. Comput, 21, 1
Butler, K. 1984, PhD thesis, University of London, UK
Casey, A. R., Hogg, D. W., Ness, M., et al. 2016, arXiv:1603.03040
Claret, A., & Torres, G. 2019, ApJ, 876, 134
Gaia Collaboration, Prusti, T., de Bruijne, J. H. J., et al. 2016, A&A, 595, A1
Danielski, C., Brucalassi, A., Benatti, S., et al. 2021, ExA, 2021, 1
de Jong, R. S., Agertz, O., Berbel, A. A., et al. 2019, Msngr, 175, 3
De Silva, G. M., Freeman, K. C., Bland-Hawthorn, J., et al. 2015, MNRAS, 449, 2604
Deng, L.-C., Newberg, H. J., Liu, C., et al. 2012, RAA, 12, 735
Edelmann, P. V. F., Ratnasingam, R. P., Pedersen, M. G., et al. 2019, ApJ, 876, 4
Gebruers, S., Straumit, I., Tkachenko, A., et al. 2021, A&A, 650, A151
Giddings, J. 1981, PhD thesis, University of London, UK
Gilmore, G., Randich, S., Asplund, M., et al. 2012, Msngr, 147, 25
Gunn, J. E., Siegmund, W. A., Mannery, E. J., et al. 2006, AJ, 131, 2332
Horst, L., Edelmann, P. V. F., Andrássy, R., et al. 2020, A&A, 641, A18
Howell, S. B., Sobeck, C., Haas, M., et al. 2014, PASP, 126, 398
Hubeny, I., & Lanz, T. 1995, ApJ, 439, 875
Kollmeier, J. A., Zasowski, G., Rix, H.-W., et al. 2017, arXiv:1711.03234
Kreidberg, L. 2017, Exoplanet Atmosphere Measurements from Transmission Spectroscopy and Other Planet Star Combined Light Observations (Cham: Springer), 1
Lenorzer, A., Mokiem, M. R., de Koter, A., & Puls, J. 2004, A&A, 422, 275
Limbach, M. A., Schmidt, L. M., DePoy, D. L., et al. 2020, in Ground-based and Airborne Instrumentation for Astronomy VIII, ed. C. J. Evans, J. J. Bryant, & K. Motohara, 1634
Liu, L., Jiang, H., He, P., et al. 2019, arXiv:1908.03265
Luo, F., Zhao, Y.-H., Li, J., Guo, Y.-J., & Liu, C. 2021, RAA, 21, 272
Massey, P., Zangari, A. M., Morrell, N. I., et al. 2009, ApJ, 692, 618
Ness, M., Hogg, D. W., Rix, H. W., Ho, A. Y. Q., & Zasowski, G. 2015, ApJ, 808, 16
Nidever, D. L., Holtzman, J. A., Allende Prieto, C., et al. 2015, AJ, 150, 173
Nieva, M. F., & Przybilla, N. 2007, A&A, 467, 295
O'Briain, T., Ting, Y.-S., Fabbro, S., et al. 2021, ApJ, 906, 130
Pápics, P. I., Tkachenko, A., Van Reeth, T., et al. 2017, A&A, 598, A74
Pedersen, M. G., Aerts, C., Pápics, P. I., et al. 2021, NatAs, 5, 715
Pedersen, M. G., Aerts, C., Pápics, P. I., & Rogers, T. M. 2018, A&A, 614, A128
Piskunov, N., & Valenti, J. A. 2017, A&A, 597, A16
Poggio, E., Drimmel, R., Cantat-Gaudin, T., et al. 2021, A&A, 651, A104
Puls, J., Urbaneja, M. A., Venero, R., et al. 2005, A&A, 435, 669
Ramírez-Preciado, V. G., Roman-Lopes, A., Román-Zúñiga, C. G., et al. 2020, ApJ, 894, 5
Raskin, G., van Winckel, H., Hensberge, H., et al. 2011, A&A, 526, A69
Richards, G. T., Fan, X., Newberg, H. J., et al. 2002, AJ, 123, 2945
Roman-Lopes, A., Román-Zúñiga, C., Tapia, M., et al. 2018, ApJ, 855, 68

Sana, H., de Koter, A., de Mink, S. E., et al. 2013, A&A, 550, A107
Sana, H., de Mink, S. E., de Koter, A., et al. 2012, Sci, 337, 444
Serenelli, A., Weiss, A., Aerts, C., et al. 2021, A&ARv, 29, 4
Shulyak, D., Tsymbal, V., Ryabchikova, T., Stütz, C., & Weiss, W. W. 2004, A&A, 428, 993
Smee, S. A., Gunn, J. E., Uomoto, A., et al. 2013, AJ, 146, 32
Sobol, I. M. 1967, USSR Comp. Math. and Math. Phys., 7, 86
Stoughton, C., Lupton, R. H., Bernardi, M., et al. 2002, AJ, 123, 485
Strauss, M. A., Weinberg, D. H., Lupton, R. H., et al. 2002, AJ, 124, 1810
Sundqvist, J. O., Björklund, R., Puls, J., & Najarro, F. 2019, A&A, 632, A126
Thomas, J. D., Richardson, N. D., Eldridge, J. J., et al. 2021, MNRAS, 504, 5221

Ting, Y.-S., Conroy, C., Rix, H.-W., & Cargile, P. 2019, ApJ, 879, 69
Tkachenko, A. 2015, A&A, 581, A129
Tkachenko, A., Pavlovski, K., Johnston, C., et al. 2020, A&A, 637, A60
Torres, G., Andersen, J., & Giménez, A. 2010, A&ARv, 18, 67
Tsymbal, V. 1996, in ASP Conf. Ser. 108, M.A.S.S., Model Atmospheres and Spectrum Synthesis, ed. S. J. Adelman, F. Kupka, & W. W. Weiss (San Francisco, CA: ASP), 198
Valenti, J. A., & Piskunov, N. 1996, A&AS, 118, 595
Vanderspek, R. 2019, AAS Abstracts, 51, 333.12
Wilson, J. C., Hearty, F. R., Skrutskie, M. F., et al. 2019, PASP, 131, 055001
Xiang, M., Rix, H.-W., Ting, Y.-S., et al. 2021, arXiv:2108.02878
Zari, E., Rix, H. W., Frankel, N., et al. 2021, A&A, 650, A112